AD-A073 140 MASSACHUSETTS INST OF TECH LEXINGTON LINCOLN LAB F/G 20/5
RESEARCH STUDIES ON NEODYMIUM PENTAPHOSPHATE MINIATURE LASERS.(U)
SEP 78 S R CHINN F19628-78-C-0002

UNCLASSIFIED ESD-TR-78-392 NL

END
DATE FILMED
79
DDC

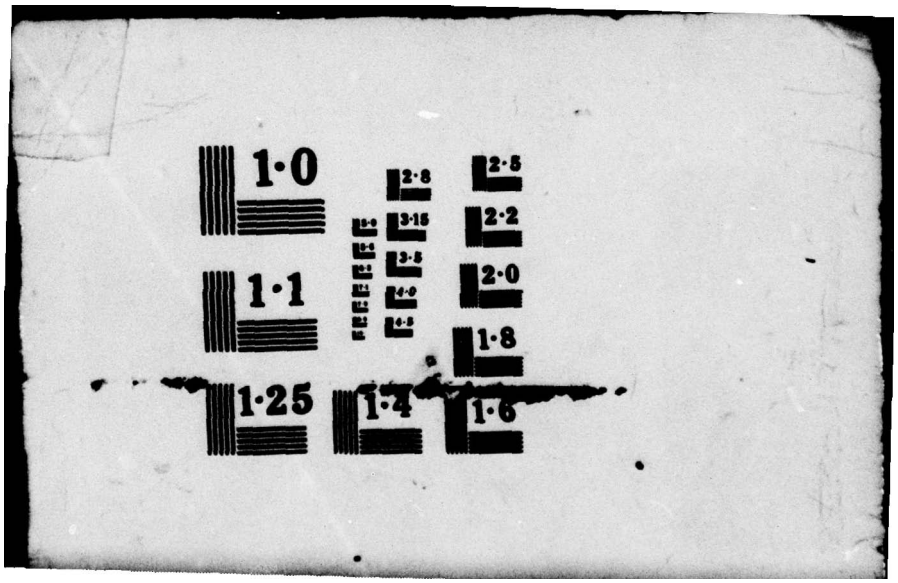
1·0
1·1
1·25
1·4
1·6
1·8
2·0
2·2
2·5
2·8
3·15
3·5
4·0

MASSACHUSETTS INSTITUTE OF TECHNOLOGY

LINCOLN LABORATORY

RESEARCH STUDIES ON NEODYMIUM PENTAPHOSPHATE MINIATURE LASERS

S. R. CHINN

Group 82

FINAL REPORT

30 SEPTEMBER 1978

LEXINGTON MASSACHUSETTS

ABSTRACT

The thermal conductivity and specific heat of NdP_5O_{14} have been measured using a dynamic electrical heating technique. The values of the thermal conductivity tensor elements (in W/cm-K) are $\Lambda_a = 3.10 \times 10^{-2}$, $\Lambda_b = 9.66 \times 10^{-3}$, and $\Lambda_c = 1.40 \times 10^{-2}$. The specific heat is 0.141 cal/g-K, in excellent agreement with the value of 0.139 cal/g-K that was measured by differential scanning calorimetry.

Using the experimentally measured thermal properties, we have calculated the time-dependent heating effects of typical flash-lamp-excited round and rectangular laser rods. With repetition rates limited to ±10 ppm, simple conductive cooling by an ambient-temperature heat-sink should be adequate.

Computer simulation of the flash-lamp-excited NPP laser has been carried out by numerical solution of the laser rate equations. With 1 J electrical input, typical calculated output energies are 24 mJ for normal-mode operation and 10 mJ for passively Q-switched operation. Optimum Q-switch absorption and output mirror transmission have also been calculated.

Experimental studies of such lasers have been made with varying laser rod size and laser resonator parameters. With the largest rod, $2 \times 2 \times 20$ mm^3, we have obtained 72 mJ output with 3.4 J input, in a normal-mode confocal resonator. Passive Q-switching of $2 \times 2 \times 10$-mm^3 rods in a hybrid unstable resonator has produced 5 mJ near-field output (2 J input) in a 6-nsec pulse, with 3.9 mJ collected in a 3.1-mrad far-field aperture.

PREFACE

This work was performed by Lincoln Laboratory, a center for research operated by Massachusetts Institute of Technology. The work was sponsored by the United States Army Electronic Research and Development Command, Combat Surveillance and Target Acquisition Laboratory under Air Force Contract F19628-78-C-0002. Mr. John G. Gualtieri was the Contracting Officer's Representative for USAERADCOM.

Dr. Stephen R. Chinn was responsible for the preparation of this Final Technical Report of work performed at Lincoln Laboratory. Mr. William E. Barch provided assistance in the experimental measurements and Mrs. Barbara J. Palm aided in the computer programming. The crystal samples used in the thermal conductivity measurements were prepared by Mr. Stephen Duda, and the electrode patterns and leads were fabricated by the Microelectronics Group (87) of Lincoln Laboratory. The Nd pentaphosphate crystal material and laser rods used in this study were provided by Dr. Walter K. Zwicker of Philips Laboratories, Briarcliff Manor, New York. The growth and fabrication of these rods is described by Dr. Zwicker in the final report prepared for USAERADCOM, "*Development of Neodymium Pentaphosphate* Laser Rods," Contract Number DAAB07-77-C-2154, 3 April 1978.

CONTENTS

I. INTRODUCTION

This report describes the results of research studies on neodymium pentaphosphate minature lasers. The high Nd concentration in this material (NdP_5O_{14}, abbreviated as NPP) allows effecient absorption of pump radiation and the construction of small laser devices which should be suitable for rangefinder applications. Most of the important fluorescence and optical properties of NPP have been previously measured and reported, so that our efforts were confined to two other general areas: the determination of the material's thermal properties and the evaluation of flash-lamp-excited laser performance. In Section II of this report, we describe the method and results of the measurement of the thermal conductivity and specific heat of NPP. Using these data, we also do some simple calculations to estimate the thermal limitations of NPP laser performance. In Section III, we examine the characteristics of NPP flash-lamp-excited lasers. First, the details of a computer simulation of such lasers are given, including the effects of varying the Nd concentration in the laser rod, and of incorporating a saturable-absorber Q-switch in the laser cavity. Next, the experimental results describing the operation of NPP lasers are presented. These results include operation in normal and Q-switched modes, in stable and unstable resonators, and with varying laser rod sizes. Finally, in Section IV we summarize the results, and indicate further areas of investigation of assessment of NPP as a rangefinder laser material.

All of the NdP_5O_{14} crystals and laser rods described in this report were provided by Dr. W. K. Zwicker, Philips Laboratories, Briarcliff Manor, New York.

II. THERMAL PROPERTIES

One of the problems in operation of high-energy, fast-repetition-rate pulsed lasers is heat removal from the laser rod. In order to analyze this problem, we have measured the thermal conductivity and specific heat of NPP using a recently published technique. Most of the pertinent analysis and results are given in the following Section II-A, parts (1) – (5) of which are the manuscript of an article (with W. K. Zwicker) to be published in the Journal of Applied Physics. Additional experimental details and data are found after the first part, and an elaboration of the theoretical calculations of the conductivity measurement is found in the Appendix. In Section II-B, we present some calculations on laser rod heating based on the measured thermal conductivity.

A. THERMAL CONDUCTIVITY AND SPECIFIC HEAT OF NdP_5O_{14}

1. Background

Neodymium pentaphosphate is a high-Nd-concentration material with small enough fluorescence quenching for use in miniature, efficient lasers.[1,2] Growth of crystals of NPP larger than previously available and having volumes of several cubic centimeters[3] has permitted the fabrication of rods for flash-lamp-excited lasers.[4] One objective of the further development of high-Nd-concentration lasers is to make CW devices, pumped either by lamps or by light-emitting diodes. Another goal is to increase the repetition rate and average power of the flash-lamp-pumped lasers. For either of these developments, heat removal from the laser rod is of prime concern, and the thermal conductivity of the rod must be known for proper design. We have measured the anisotropic thermal conductivity tensor and the specific heat of NPP by using a simple extension of the technique recently described by Bruce and Cannell[5] for determining the thermal conductivity and specific heat of isotropic, electrically insulating solids. The basic principle of measurement is straightforward. Two parallel metal strips are fabricated on the surface of the sample. Alternating current is passed through one strip, the heater, and the temperature-induced periodic resistance variation of the other strip, the sensor, is measured as a function of the heating frequency. From the measured data, and together with the electrical parameters for the heater and sensor and the temperature coefficient of sensor resistance, the thermal conductivity and specific heat can be found.

The theoretical relation of the thermal conductivity tensor elements to the measured data is given in Section II-A-2 below. In Section II-A-3, we briefly describe the experimental method, particularly the aspects in which it differs from the method of Ref. 5. The experimental results are presented in Section II-A-4 and discussed in Section II-A-5.

2. Theory

We have extended the theoretical calculation of Ref. 5 to allow for different thermal conductivities along the different crystallographic axes. A related derivation for transient excitation is found in Ref. 6. Since the space group of NPP is monoclinic,[7] in principle it is necessary to find a new set of principal axes along which the thermal conductivity tensor is diagonal.[8] However, the monoclinic angle β deviates from 90° by only 0.5°, so we shall make the simplification of assuming orthorhombic symmetry, with the tensor diagonal along the three nearly perpendicular crystal axes, and having components $\Lambda_i = \Lambda_a$, Λ_b, and Λ_c.

The following discussion uses the notation of Ref. 5 as closely as possible, and proceeds along similar lines, except that we first find the slightly more general three-dimensional, time-dependent Green's function (see, for example, Ref. 9). The heat-flow equation becomes

$$-\left(\Lambda_x \frac{\partial^2 T}{\partial x^2} + \Lambda_y \frac{\partial^2 T}{\partial y^2} + \Lambda_z \frac{\partial^2 T}{\partial z^2}\right) + \rho C \frac{\partial T}{\partial t} = P(x,t) \tag{1}$$

where

T = temperature

ρ = density

C = specific heat (heat capacity/unit weight)

$P(x,t)$ = power dissipation/unit volume.

The equation for the Green's function is

$$\Lambda_x \frac{\partial^2 G}{\partial x^2} + \Lambda_y \frac{\partial^2 G}{\partial y^2} + \Lambda_z \frac{\partial^2 G}{\partial z^2} - \rho C \frac{\partial G}{\partial t} = -4\pi\delta(r - r_o)\,\delta(t - t_o) \quad , \tag{2}$$

with solution

$$G(r,t) = \frac{\sqrt{\rho C}}{2\sqrt{\pi}\, t^{3/2}} \frac{u(t)}{\sqrt{\Lambda_x \Lambda_y \Lambda_z}} \exp -\left[\frac{\rho C}{4t}\left(\frac{x^2}{\Lambda_x} + \frac{y^2}{\Lambda_y} + \frac{z^2}{\Lambda_z}\right)\right] \quad . \tag{3}$$

[The function $u(t)$ is the causal unit step function.] With a power excitation density of $P_o\delta(r)\cos\omega t$ in Eq. (1), integration over time gives the solution (see Appendix)

$$T(r,t) = \frac{P_o}{4\pi}\left(\frac{x^2}{\Lambda_x} + \frac{y^2}{\Lambda_y} + \frac{z^2}{\Lambda_z}\right)^{-1/2} (\Lambda_z \Lambda_y \Lambda_z)^{-1/2}$$

$$\times \mathrm{Re}\left[\exp\left(i\omega t - \sqrt{i\omega\rho C}\sqrt{\frac{x^2}{\Lambda_x} + \frac{y^2}{\Lambda_y} + \frac{z^2}{\Lambda_z}}\right)\right] . \tag{4}$$

(Note that ω, the power radian frequency, is at twice the frequency of the actual heater current.) We now assume, as in Ref. 5, that the heat source distribution (coming from the heater strip) is a line in the plane at $z = 0$ which extends in the y direction from $y = -\infty$ to $+\infty$. The temperature in the $z = 0$ plane, at a distance d in the x direction from the line source (corresponding to the sensor strip location) is found by integrating Eq. (4) over the y coordinate. The temperature at the sensor is

$$T(d,t) = \frac{P}{\pi\sqrt{\Lambda_x \Lambda_z}} \mathrm{Re}\left[e^{i\omega t} K_o\left(\sqrt{\frac{i\omega\rho C}{\Lambda_x}}\, d\right)\right] \quad , \tag{5}$$

where K_o is a modified Bessel function of imaginary argument, and P is the heater power/unit length. In Eq. (5), we have also taken the solution for the case of a heater source on the surface of the infinite half-volume $z \leq 0$, using the same symmetry arguments as in Ref. 5.

The important point to be noted is that Eq. (5) is the same as Eq. (6) of Ref. 5 except that $(\Lambda_x \Lambda_z)^{-1/2}$ has replaced the initial factor Λ^{-1} and $(\omega\rho C/\Lambda_x)^{1/2}$ has replaced $(\omega\rho C/\Lambda)^{1/2}$ in the argument of the Bessel function. These substitutions are physically reasonable because the dynamic response of the heater-sensor pair given by the frequency-dependent Bessel function depends only on the diffusivity in the direction between them, whereas the magnitude of the

response given by the initial factor depends on the relative amounts of heat flow in both x and z directions out from the heater strip. Thus, the smaller the downward conductivity, Λ_z, the larger will be the heat flow and response in the x direction. Of course, the Λ_y component does not appear since with the assumed symmetry and infinite y extent, there is no heat flow in the y direction.

These arguments also apply to the correction factor discussed in Ref. 5 for the non-zero width of the heater and sensor strips, so that the final frequency-dependent complex voltage which is measured across the sensor is

$$V_\omega = \frac{V\beta P}{\pi\sqrt{\Lambda_x \Lambda_z}} K_o(\alpha d) \left[\frac{\sinh(\alpha w/2)}{\alpha w/2}\right]^2 \quad , \tag{6}$$

where

V = DC bias voltage across sensor

β = temperature coefficient of sensor resistance, (1/R) dR/dT

$\alpha = (i\omega\rho C/\Lambda_x)^{1/2}$

d = separation between heater and sensor strips

w = width of strips.

The magnitude of the voltage response is similar to Eq. (15) of Ref. 5, that is:

$$|V_\omega| = \frac{VP\beta}{\pi\sqrt{\Lambda_x \Lambda_z}} \left[\frac{\sinh^2(\bar{\alpha} w/2\sqrt{2}) + \sin^2(\bar{\alpha} w/2\sqrt{2})}{(\bar{\alpha} w/2)^2}\right] |K_o(\alpha d)| \quad , \tag{7}$$

where $\bar{\alpha} = (\omega\rho C/\Lambda_x)^{1/2}$ and the quantity Λ has become $\sqrt{\Lambda_x \Lambda_z}$.

For various crystal orientations with respect to the heater and sensor strips, the appropriate components $\Lambda_i = \Lambda_a, \Lambda_b, \Lambda_c$ are used in the above equations, assuming the simple geometry of principal axes oriented parallel and perpendicular to the strips.

3. Experimental Procedure

The measurement apparatus differed only in minor details from that described in Ref. 5. For example, we used an additional two-phase lock-in amplifier to monitor the heater current.

The sensor temperature coefficient β was found by heating each sample and measuring R over the range from 23° to 50°C. Polynomial regression was used to obtain the best fit to the data and to determine β = (1/R) dR/dT at the temperature of interest, 27°C.

The material used for heater and sensor strips was sputtered Ni, 500 Å thick. The strip patterns were defined by conventional masking and photolithographic techniques, and the unwanted Ni areas were removed either by chemical etching or film-parting. A layer of Au was evaporated over the contact pads at the ends of the two strips, and 0.001-in.-dia. Au bonding wires were attached to the contact pads, using acoustic bonding with silver-epoxy support, or just silver-epoxy alone. In all cases, the ratio of heater-to-sensor resistance was the same as the ratio of heater-to-sensor length, showing that the external connection resistances were negligible. Figure 1 is a photomicrograph of a typical strip pattern, with the external bonding wires removed. The strip patterns were generally smaller than those of Ref. 5, with minimum lengths of 2.5 mm, widths of ~4 μm, and separations ~33 μm.

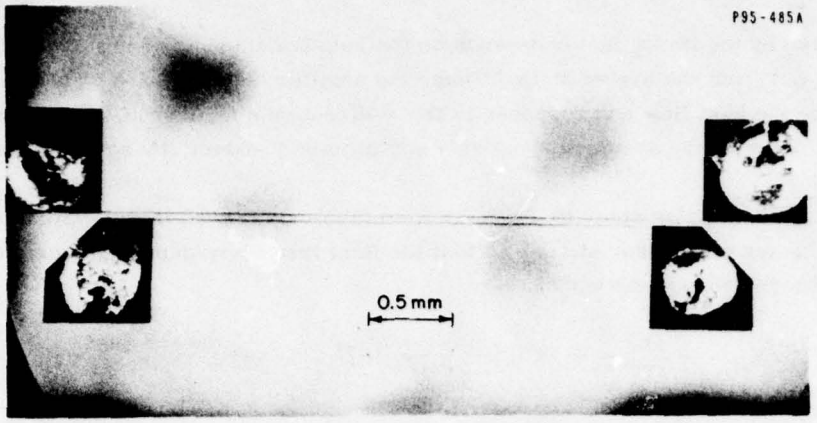

Fig. 1. Photomicrograph of heater and sensor strips with bonding pads, on a cleaved b face of NPP (the bonding wires have been removed). The heater (top) is 3 mm long, and the sensor (bottom) is 2.5 mm long. The strips are 4 μm wide, 33 μm apart, and run parallel to the a direction.

All samples were cut or cleaved from the same NPP crystal. To determine the three thermal conductivity tensor elements and the specific heat, three different orientations were used. The results for samples of the same orientation agreed within a few percent, even with considerable variation in strip parameters and power dissipation. The thermal properties were derived from the results for the one sample of each orientation that gave voltage versus frequency data showing the smallest deviation from the best-fit theoretical curves. Sample M1 had a polished c face with the metal strips in the a (y) direction. In this case, $\Lambda_x = \Lambda_b$ and $\Lambda_z = \Lambda_c$. Sample M2 also had a polished c face, but with orthogonal strip orientation, i.e., $\Lambda_x = \Lambda_a$ and $\Lambda_z = \Lambda_c$. Sample M3 had a cleaved, step-free b face with strips in the a direction, giving $\Lambda_x = \Lambda_c$ and $\Lambda_z = \Lambda_b$.

4. Results

For each sample, data at 27°C were obtained over a range of roughly two orders of magnitude in both the heater frequency and sensor voltage response. A best fit to the data was obtained by varying the two independent parameters $\sqrt{\Lambda_x \Lambda_z}$ and $\rho C/\Lambda_x$ to minimize the least-squares difference between the logarithm of the measured values of $|V_\omega|$ and the logarithm of the right side of the theoretical expression, Eq. (7). (This was done to ensure comparable, although smaller, weighting of the high-frequency points, where the absolute voltage response is smallest.) No weighting was carried out to compensate for frequency-dependent noise.[5] Typically, the largest deviation between the measured and calculated values of $|V_\omega|$ was ~1.5 percent. A set of representative data (for M3) is shown in Fig. 2, with its best-fit curve. The peak value of $|V_\omega|$ is plotted as a function of $f = \omega/2\pi$, the heating frequency (twice the current drive frequency). For this particular set of data, the experimental parameters were

$V = 0.869$ V

$P = 2.07$ mW/cm

$\beta = 1.745 \times 10^{-3}$ K^{-1}

$w = 4.67 \times 10^{-4}$ cm

$d = 3.27 \times 10^{-3}$ cm.

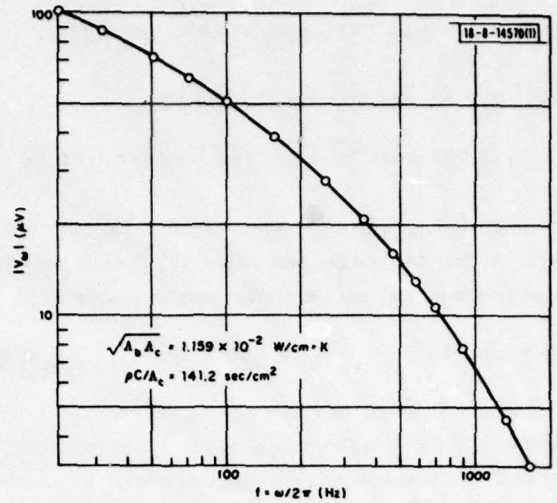

Fig. 2. Sensor voltage response $|V_\omega|$ as a function of heater frequency $f = \omega/2\pi$ for NPP sample M3. Experimental parameters are given in the text. The open circles are the data points, and the solid curve is calculated using the indicated best-fit parameters for $\sqrt{\Lambda_b \Lambda_c}$ and $\rho C/\Lambda_c$.

The two dependent parameters, $\sqrt{\Lambda_x \Lambda_z}$ and $\rho C/\Lambda_x$, obtained for each of the three orientations, are:

Sample	$\sqrt{\Lambda_i \Lambda_j}$ (W/cm-K)	(diffusivity)$^{-1}$ (sec-cm^{-2})
M1	$\sqrt{\Lambda_b \Lambda_c} = 1.172 \times 10^{-2}$	$\rho C/\Lambda_b = 204.9$
M2	$\sqrt{\Lambda_a \Lambda_c} = 1.713 \times 10^{-2}$	$\rho C/\Lambda_a = 94.3$
M3	$\sqrt{\Lambda_b \Lambda_c} = 1.159 \times 10^{-2}$	$\rho C/\Lambda_c = 141.2$

The uncertainty in the values for $\sqrt{\Lambda_i \Lambda_j}$ is about ±2 percent, and arises from the cumulative errors in measuring $|V_\omega|$, P, and β. The diffusivities, $\Lambda_i/\rho C$, are independent of the absolute system response calibration factors. We estimate that the diffusivities are accurate to about ±1 percent, reflecting the goodness of fit to the shape of the $|V_\omega(f)|$ curve. (On the logarithmic plot, the initial multiplicative factor shifts the curve without changing its shape.) The thermal conductivity ratios Λ_i/Λ_j can be found from the diffusivities without knowledge of C or absolute system response factor.

The above data are redundant in that $\sqrt{\Lambda_b \Lambda_c}$ is obtained for two orientations; the two values agree to within 1 percent, confirming the overall calibration accuracy. For the further data reduction, we use the average value $\sqrt{\Lambda_b \Lambda_c} = 1.166 \times 10^{-2}$ W/cm-K. The value of $\Lambda_a/\Lambda_b = 2.173$ found by taking the ratio of diffusivities agrees to better than 1 percent with value $\Lambda_a/\Lambda_b = 2.158$ found by taking the square of the ratio of $\sqrt{\Lambda_a \Lambda_c}$ to $\sqrt{\Lambda_b \Lambda_c}$ from the Λ factors.

Combining the $\sqrt{\Lambda_b \Lambda_c}$ and diffusivity results for samples M1 and M3, we can calculate the specific heat (per unit volume), ρC, as follows:

$$\Lambda_b \Lambda_c = (1.66 \times 10^{-2})^2 = (\rho C/204.9) \times (\rho C/141.2) \quad ,$$

giving $\rho C = 1.98$ J/cm^3-K. Similarly, for M2 and M3,

$$\Lambda_a \Lambda_c = (1.713 \times 10^{-2})^2 = (\rho C/94.3\ ) \times (\rho C/141.2) \quad ,$$

also giving $\rho C = 1.98$ J/cm^3-K. The high-temperature Dulong-Petit limiting value for ρC in NPP is 3.21 J/cm^3-K. Using the measured value of ρC with the diffusivity parameters gives the following values of the thermal conductivity tensor elements:

$$\Lambda_a = 2.10 \times 10^{-2} \qquad \Lambda_b = 9.66 \times 10^{-3} \qquad \Lambda_c = 1.40 \times 10^{-2} \text{ W/cm-K} \quad .$$

The density of NPP calculated from its lattice parameters[7] is 3.365 g/cm^3, which gives the specific heat (per unit weight) $\mathcal{C} = 0.141$ cal/g-K.

Using small pieces from the same NPP single crystal as above, we also measured the specific heat directly with a DuPont 900 Differential Thermal Analyzer equipped with a differential scanning calorimetry (DSC) cell. Powders of Zn and Al were used as specific-heat calibration materials. The directly measured specific heat of NPP was $\mathcal{C} = 0.139 \pm 0.002$ cal/g-K, in excellent agreement with the value obtained by the electrical dynamic measurement.

5. Discussion

The thermal conductivity of NPP is low compared with that of YAG, one of the better heat-conducting laser hosts. Even the highest component in NPP, $\Lambda_a = 2.10 \times 10^{-2}$ W/cm-K, is only one-sixth of the value for YAG, 0.13 W/cm-K (Ref. 10). However, this does not rule out NPP for CW or high-repetition-rate lasers, since rods of NPP will typically be much smaller than their Nd:YAG counterparts. Even in very small Nd:YAG laser systems, the rod diameter is commonly at least 3 mm to ensure efficient absorption of pump radiation. Since NPP has 30 times higher Nd concentration than Nd:YAG with standard 1% Nd doping, smaller NPP rod diameters can be used. For example, a 1-mm^2 rod was used in Ref. 4. The temperature rise at the rod center, for a given heat-sink surface temperature, varies as the square of the rod dimension and inversely with the thermal conductivity.[11] By using a NPP rod with about $1/\sqrt{6} \sim 0.4$ times the transverse dimension of a Nd:YAG rod, comparable cooling can be achieved.

The thermal conductivity of NPP is rather anisotropic, with $\Lambda_a:\Lambda_c:\Lambda_b = 2.17:1.45:1$. This thermal anisotropy is consistent with both the mechanical properties of NPP crystals and the microscopic crystal structure. The lowest conductivity direction is perpendicular to the easy-cleavage b plane, and the highest conductivity is in the a direction, along the structurally close-knit ribbons of phosphate groups. If cooling of the laser rod is nonuniform, over only part of the rod surface, it is therefore important to ensure that the heat flow is in the a direction.

The present technique for electrical dynamic measurement of the thermal conductivity and specific heat is quite simple and convenient. For measurement of these properties in NPP, in particular, it afforded several advantages:

(a) The sample size could be quite small, with measurement surfaces about 2 mm × 4 mm and a minimum thickness of only about 2 mm.

(b) All three thermal conductivity tensor elements could be determined using only the two b and c crystal surfaces for measurement. In a conventional direct heat flow measurement, it is desirable to have smooth, flat sample surfaces to minimize thermal impedance across the interfaces. Measurement of Λ_a by the direct technique would have required a polished a surface, which is difficult to prepare.

(c) The specific heat was determined along with Λ_i, providing a parameter which could be compared with the calorimetrically measured value for confirmation of the experimental accuracy.

The transient method of Ref. 6 would also offer these advantages, but experimentally it would probably be more difficult to obtain accurate measurements of the low-level time-dependent voltage response than the steady-state frequency-dependent response. An interesting technique for determining the thermal diffusivity by measuring laser-induced temperature distributions[12] might also be applicable, but would be complicated by the fluorescence properties of NPP.

6. Additional Experimental Details and Data

Block diagrams of the experimental apparatus are shown in Figs. 3 and 4. In Fig. 3 is given the setup for determining the sensor temperature coefficient. The temperature controller stabilizes the sample (and sensor) temperature, which is measured by a calibrated Pt resistance and digital ohmmeter. The resistance of the sensor strip is measured using a DC current source set at 100 μA and measuring the voltage with the digital voltmeter. The resistance values were measured from room temperature to ~50°C.

The apparatus for measuring the thermal conductivity is shown in Fig. 4. The low-frequency function generator provides the AC power to the heater resistance element, R_H. A calibrated 10Ω resistance in series with the heater is used to determine the current through R_H, and hence the heating power. A battery-powered current source provides the DC bias to the sensor element, R_S, and the AC temperature-induced voltage component is amplified and detected at twice the heater frequency by the lock-in amplifier.

The experimental parameters for the samples M1 and M2, not given above, are:

	M1	M2	
V	0.681	1.404	V
P	1.73	3.17	mW/cm
β	1.80×10^{-3}	1.35×10^{-3}	K^{-1}
w	8.19×10^{-4}	4.68×10^{-4}	cm
d	6.35×10^{-3}	3.27×10^{-3}	cm

The experimental data for M1 and M2 are shown in Figs. 5 and 6, with the best-fit curves and parameters $\sqrt{\Lambda_i \Lambda_j}$ and $\rho C/\Lambda_i$ for each case.

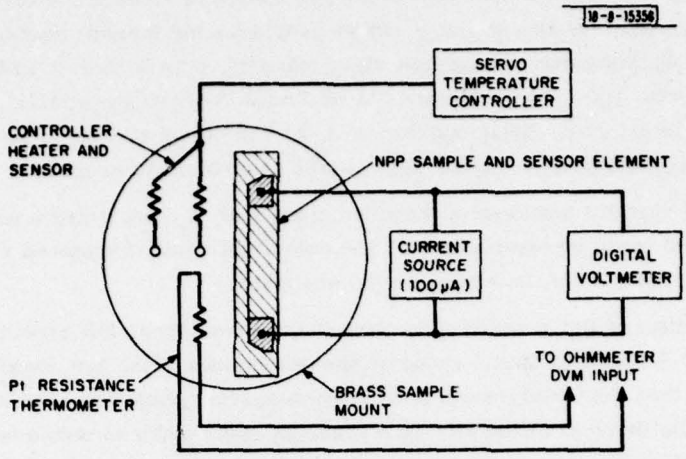

Fig. 3. Experimental apparatus for measuring temperature coefficient of sensor element on NPP sample.

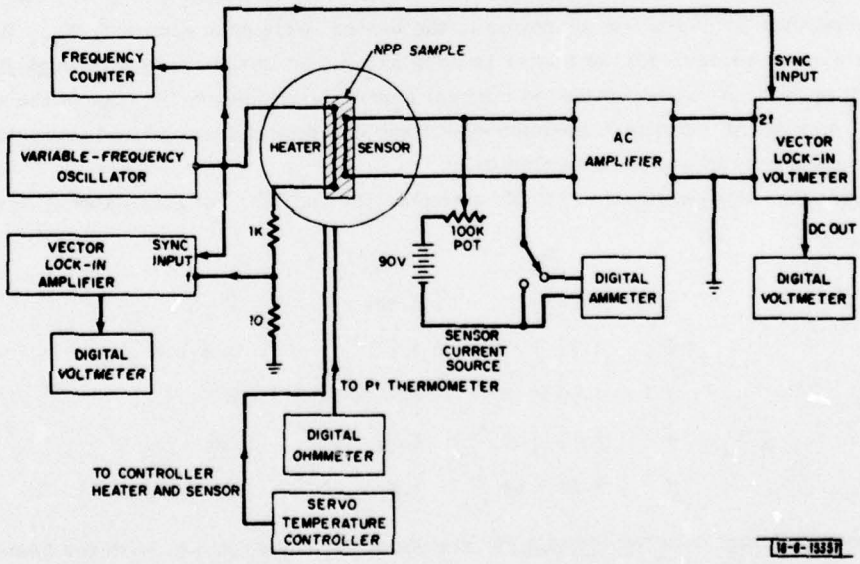

Fig. 4. Experimental apparatus for measuring thermal conductivity and specific heat of NPP.

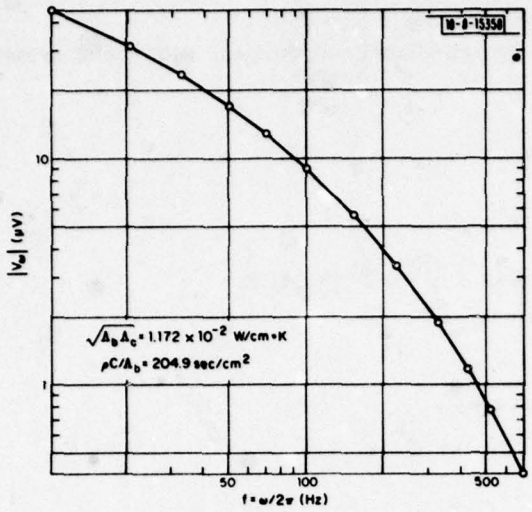

Fig. 5. Sensor voltage response as a function of heater frequency for NPP sample M1.

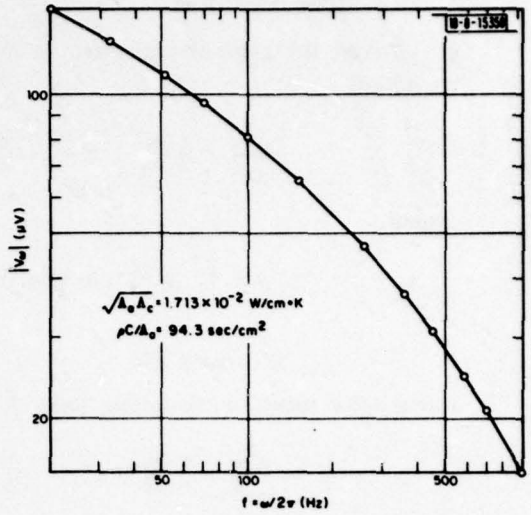

Fig. 6. Sensor voltage response as a function of heater frequency for NPP sample M2.

B. TIME-DEPENDENT HEATING EFFECTS

1. Statement of the Problem

The problem that is addressed in this section is the determination of the temperature rise in a pulsed NPP laser, and the resulting limitations on pump energy or repetition rate. In principle, such calculations can be done as accurately as desired, but require a good knowledge of the excitation geometry and rod cooling parameters, and a subsequent numerical solution of the heat-diffusion equation. For the present, we are primarily concerned with an easily obtained semi-quantitative answer to the heating problem, so that we restrict ourselves to simple models for which analytic solutions can be found.

First, the experimental situations which we have dealt with, and presumably which would be encountered in the laser rangefinder, are for uniform transverse mode structure across the laser rod. This could arise either from multimode alignment of a stable resonator, or a simple uniform transverse mode of an unstable resonator. For this reason, we choose the initial thermal excitation to be uniformly distributed over the rod cross section. This is probably not the case, due to nonuniform absorption of the pump radiation, but even a nonuniform temperature distribution would have to be integrated over the laser mode profile to give the total average heating effect. Also, the details of finding the nonuniform excitation profile and of then calculating the time evolution would be quite complicated.

Second, we approximate the flash-lamp excitation to have a delta-function time dependence. This is probably a good approximation because, as we shall see, the lamp pulse duration, ~50 μsec, is very much shorter than any characteristic heat diffusion time in these lasers.

Third, we shall treat only simple rod geometries. First, we examine the cylindrical rod with isotropic conductivity and uniform heat-sinking. Next, we treat the problem of one-dimensional heat flow across a slab. The actual case of a rectangular rod, heat sunk on one surface and pumped primarily on the opposite face, represents a combination of these two cases.

2. Cylindrical Rod

Taking the Laplace transform of Eq. (1), in cylindrical coordinates, with radial symmetry, we obtain

$$\frac{d^2v}{dr^2} + \frac{1}{r}\frac{dv}{dr} - q^2 v = -\frac{1}{\Lambda} A(p) \tag{8}$$

where

$$v = \int_0^\infty e^{-pt}\, T(r,t)\, dt \quad , \quad A(p) = \int_0^\infty e^{-pt}\, P(r,t)\, dt$$

$$q^2 = p(\rho C/\Lambda) \quad .$$

For a delta-function excitation, with $\int A(t)\, dt = b$,

$$\frac{d^2v}{dr^2} + \frac{1}{r}\frac{dv}{dr} - q^2 v = -\frac{b}{\Lambda} \quad , \tag{9}$$

with the form of solution[8]

$$v = c_1 + c_2 I_o(qr) + c_3 K_o(qr) \quad . \tag{10}$$

Since v is finite at r = 0, $c_3 = 0$. The other boundary condition is that the temperature be constant (here set to zero) at the boundary r = a. The boundary conditions and Eq. (9) give

$$v = \frac{b}{\rho C}\frac{1}{p}\left[1 - \frac{I_o(qv)}{I_o(qa)}\right] \quad . \tag{11}$$

The inverse transform is

$$T(r,t) = \left(\frac{b}{\rho C}\right)\frac{1}{2\pi i}\int_{-i\infty}^{+i\infty}\left[\frac{1}{\lambda} - \frac{I_o(\mu r)}{\lambda I_o(\mu a)}\right] e^{\lambda t}\, d\lambda \quad , \tag{12}$$

with $\mu = \sqrt{\lambda\rho C/\Lambda}$, which is evaluated by finding the residues of the contour integral in the left-half complex plane. The result is

$$T(r,t) = \frac{2}{a}\frac{b}{\rho C}\sum_{n=1}^{\infty} e^{-\Lambda/\rho C\alpha_n^2 t}\,\frac{J_o(\alpha_n r)}{\alpha_n J_1(\alpha_n a)} \quad , \tag{13}$$

where α_n are the zeros of the Bessel function given by $J_o(\alpha_n a) = 0$. In dimensionless units

$$u = r/a$$

$$\tilde{t} = t\,\frac{\Lambda}{\rho C a^2} \quad ,$$

$$T(u,\tilde{t}) = \frac{2b}{\rho C}\sum_{n=1}^{\infty}\frac{J_o(u_n u)}{u_n J_1(u_n)}\, e^{-u_n^2\tilde{t}} \quad , \quad J_o(u_n) = 0 \quad . \tag{14}$$

The temperature is plotted as a function of normalized spatial coordinate u in Fig. 7, at fixed intervals from $\tilde{t}$ = 0.05 to 0.50 in increments of 0.05, and has itself been normalized by the

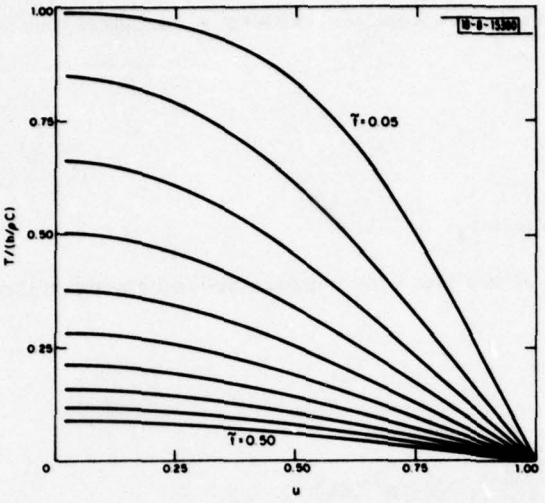

Fig. 7. Temperature as a function of radial distance for different times after a uniformly distributed heat impulse in a cylindrical rod. All parameters are normalized as explained in the text.

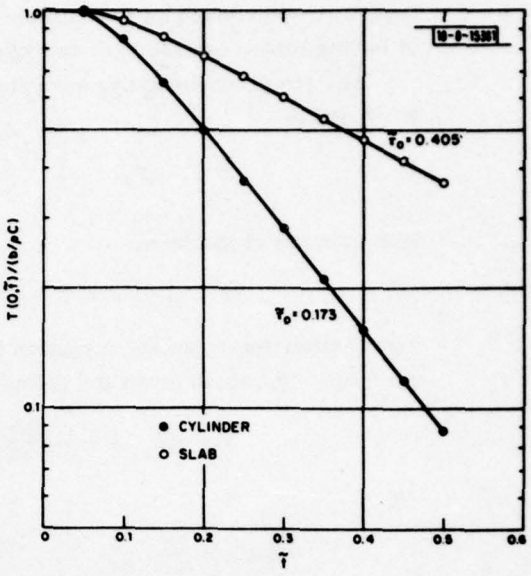

Fig. 8. Logarithmic dependence of temperature at rod center with time (solid circles). The time-dependence for the rectangular slab is also shown (open circles), with both limiting decay times being indicated.

parameter ($b/\rho C$). After a short interval ($\tilde{t} > 0.2$), the temperature at the rod center is dominated by the lowest order normalized decay constant, $\tilde{\tau}_o = 1/u_o^2 = 0.173$, so that this single exponential decay is a good approximation to the subsequent temperature evolution, as shown in Fig. 8.

Taking some typical parameters, a = 1 mm and an average diffusivity $\Lambda/\rho C = 7.5 \times 10^{-3}$ cm^2/sec, the actual decay time $\tau_o = 0.23$ sec. The initial temperature rise is $b/\rho C$ which can be estimated from the pumping parameters. Of the 1 J of electrical energy into the flashlamp, approximately 60 percent is radiated, and we will assume that half of this is coupled into the laser rod. On the order of 20 percent of this broadband radiation is absorbed by the Nd^{3+} ions, giving $b \simeq 60$ mJ. Approximately 10 mJ might be emitted as laser radiation, giving a net value of B = 50 mJ of thermal energy input. Since $\rho C \simeq 2$ J/cm^3-K, the temperature rise is

$$\Delta T = \frac{B}{(\pi a^2 \ell)} \frac{1}{\rho C} = \frac{0.05 \text{ J}}{\pi (0.1)^2 \times 1 \text{ cm}^3} \frac{1}{2 \text{ J/cm}^3\text{-K}} = 0.8 \text{ K} \quad .$$

In a periodic pulse train with period T, with simple exponential decay, the temperature will increase by a factor of $[1 - \exp(-T/\tau_o)]^{-1}$, which should be negligible for $T > 4\tau_o \simeq 1$ sec. Of course, this calculation neglects convective heating by the lamp, or other types of radiation absorption processes in the rod such as direct UV, atomic, or infrared lattice absorptions.

3. Rectangular Rod

In examining the case of the rectangular laser rod, we shall simplify the situation and assume that no heat flow occurs across surfaces which are not contacted to the heat sink. This

transforms the problem to a simple one-dimensional model, and we will examine the situations of having either one face, or two opposite faces cooled.

The simple rectangular-coordinate heat flow equation, with no y variation, corresponding to Eq. (9) is

$$\frac{\partial^2 v}{\partial x^2} - q^2 v = -\frac{b}{\Lambda} \quad , \tag{15}$$

with solution of the form

$$v = c_1 \sinh qx + c_2 \cosh qx + c_3 \quad . \tag{16}$$

First, apply the boundary condition that at two faces the temperature is constrained to be zero, $v(x = \pm L) = 0$, which gives the solution

$$v = \frac{b}{\rho C p} \left[1 - \frac{\cosh qx}{\cosh qL}\right] \quad , \tag{17}$$

and

$$T(x,t) = \left(\frac{b}{\rho C}\right) \frac{1}{2\pi i} \int_{-i\infty}^{+i\infty} \left[\frac{1}{\lambda} - \frac{\cosh(\mu x)}{\lambda \cosh(\mu L)}\right] e^{\lambda t}\, d\lambda \quad , \tag{18}$$

again with $\mu = \sqrt{\lambda \rho C / \Lambda}$. Evaluation of the contour integral by summation of the residues results in

$$T(x,t) = \frac{2b}{\rho C} \cdot \frac{2}{\pi} \sum_{n=0}^{\infty} (-1)^n e^{-u_n^2 \tilde{t}} \frac{\cos(u_n u)}{(2n+1)} \tag{19}$$

where

$$u = x/L$$

$$u_n = (n + 1/2)\,\pi$$

$$\tilde{t} = \frac{\Lambda}{\rho C} \frac{t}{L^2} \quad .$$

At this point, we can also find the solution for the slab with only one face fastened to the heat sink, and no heat flow across the opposite face. It is convenient to shift the coordinate system so that the boundary conditions are $v(2L) = 0$ and $(\partial v/\partial x)\,(0) = 0$. With these constraints

$$c_3 = \frac{b}{\rho C p}$$

$$c_1 \sinh 2qL + c_2 \cosh 2qL + c_3 = 0$$

$$c_1 q \cosh(0) + c_2 q \sinh(0) = 0$$

giving

$$v = \frac{b}{\rho C p} \left[1 - \frac{\cosh qx}{\cosh 2qL}\right] \quad . \tag{20}$$

As might be expected from symmetry arguments, Eq. (20) and its inverse transform are identical to Eqs. (17) and (19) with the replacement of the dimension L by 2L, or

$$u = x/2L$$

$$u_n = (n + 1/2)\,\pi$$

$$\tilde{t} = \frac{\Lambda}{\rho C}\,\frac{t}{4L^2} \quad .$$

The time evolution of the normalized temperature is shown in Fig. 9. In this case, the asymptotic normalized decay constant is $\tilde{\tau}_o = 1/u_o^2 = (\pi/2)^{-2}$ (Fig. 8), and $\tau_o = (\rho C/\Lambda)\,(2L)^2\,(2/\pi)^2$. For a rod 2 mm thick (2L = 0.2 cm), with $\rho C/\Lambda_a = 94.3$ sec/cm^2, the decay time is $\tau_o = 1.53$ sec.

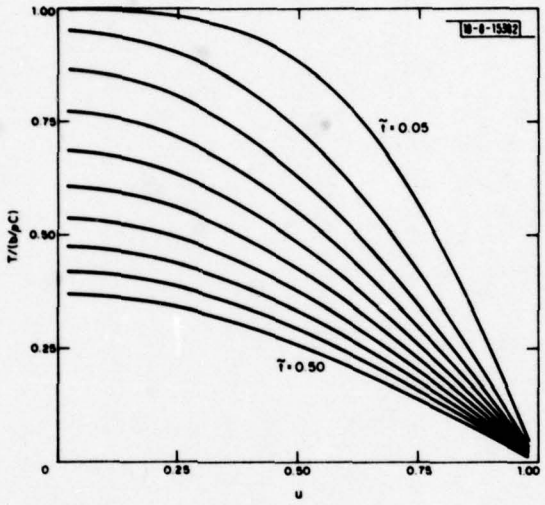

Fig. 9. Temperature as a function of distance (either from slab center, or uncooled slab face) for different times after a uniformly distributed heat pulse in the slab, for rectangular rod with no transverse heat flow. The boundary conditions determine the normalization parameters.

The initial temperature rise is

$$\Delta T = \frac{B}{(2L)^2\,l}\,\frac{1}{\rho C} = \frac{0.05\ \text{J}}{(0.2)^2 \times 1\ \text{cm}^3}\,\frac{1}{2\ \text{J/cm}^3\text{-K}} = 0.63\ \text{K} \quad .$$

Although at first glance, this one-dimensional problem may seem like an extreme simplification, it probably is more accurate a model than the uniformly cooled cylindrical rod. Irrespective of the actual energy input to the rod, the thermal time constant will be on the order of 1 or 2 sec. With very close coupling to the flash lamp, convective heating may also be important, as well as overall conductive heating of the entire laser head assembly. Therefore, unless a more elaborate cooling method is used, simple conductive cooling of one rod face will probably limit the rangefinder repetition rate to about 10 ppm.

III. NPP FLASH-LAMP-EXCITED LASER STUDIES

A. COMPUTER SIMULATION

1. Description of the Problem

In an effort to improve our understanding of the operation of flash-lamp-excited NPP lasers, we have carried out numerical analysis of these devices by means of computer solution of the laser rate equations. Such simulation should be useful for several reasons:

(a) We should obtain a semi-quantitative estimate of expected device efficiencies under different operating conditions to compare with our experimental results.

(b) We should have a guide for experimental studies and for optimizing the actual laser parameters by studying the simulated effects of varying Q-switch saturable absorber and output-coupling parameters.

(c) We can calculate the effects of reducing the Nd concentration, a variable which we have not yet been able to change experimentally because of fabrication difficulties with lower Nd concentration laser rods.

The approach we have taken is straightforward. Given the lamp emission spectrum for a certain pump energy, the laser rod excitation is calculated, and the coupled photon and population inversion rate equations are solved in the low-gain approximation, with and without the presence of a saturable absorber in the laser cavity. Many forms of the rate equations are found in the published literature, but we shall derive the equations used in our numerical analysis, indicating the approximations used and our nomenclature.

One simplification which we use is the assumption of a uniform laser mode profile. This probably corresponds closely to the actual situation of either a highly multimode output, where the intensity of many different-order Hermite-Gaussian modes gives a quasi-uniform distribution across the laser rod, or of the single lowest order mode of an unstable resonator, which is designed with the purpose of providing a nearly uniform mode across the gain medium. The effects of having a given nonuniform mode profile could be included in the calculations, but with much more complicated and time-consuming numerical integration.

The next approximation concerns the nature of the flash-lamp excitation. For numerical purposes, the time dependence of the light output is characterized by a Gaussian pulse. The calculated shape for a simple LC-flash-lamp circuit is somewhat different,[13] but the presence of a saturating inductance in our series trigger transformer smoothes out the pulse shape so that it does superficially resemble a Gaussian. In any event, this should not be a critical factor in determining the integrated output energies. Another simplification, which should be fairly accurate, is the characterization of the lamp output by a blackbody spectral distribution. With the small-bore lamps being used, large peak current densities on the order of 7000 A/cm^2 produce a nearly blackbody continuum output, rather than the narrow line emission found at low current densities. In principle, the temperature used in calculating the spectral distribution varies during the pulse, giving a distribution varying with time. To avoid this complication, we assume that the color temperature (determined by the electrical input energy and pulse duration) is constant, and that the instantaneous output power is proportional to the discharge Gaussian pulse amplitude.

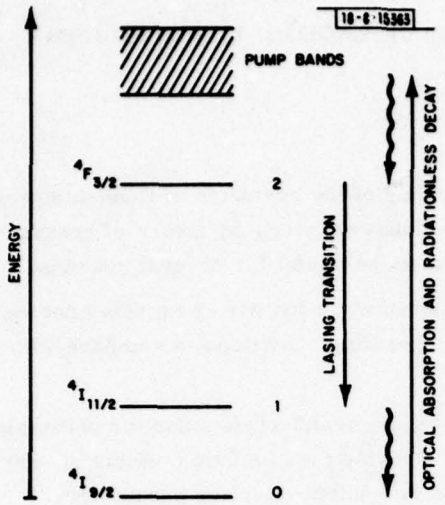

Fig. 10. Simplified energy-level diagram of Nd^{3+} indicating the levels used in the rate equations. The crystal-field split manifolds are indicated as single levels, and the separations are not to scale.

2. Derivation of Laser Rate Equations

The Nd^{3+} ion is modeled by the simplified energy level diagram in Fig. 10. The population rate equation is

$$\frac{dN_2}{dt} = -\frac{N_2}{\tau} - \frac{I}{I_s}\frac{N_2}{\tau} + \frac{I}{I_s}\frac{\sigma^A}{\sigma^B}\frac{N_1}{\tau} + \beta N_0 \tag{21}$$

where

$N_2 = {}^4F_{3/2}$ population density

$N_1 = {}^4I_{11/2}$ population density

N_0 = ground-state population density $\simeq$ N = Nd concentration

βN_0 = excitation rate (per unit volume)

$\tau = {}^4F_{3/2}$ fluorescence lifetime

I = laser mode intensity

I_s = laser saturation intensity = $h\nu/\sigma^B\tau$

σ^B = population weighted ${}^4F_{3/2} \rightarrow {}^4I_{11/2}$ emission cross section

σ^A = population weighted ${}^4I_{11/2} \rightarrow {}^4F_{3/2}$ absorption cross section.

In reducing the equations for the three levels (0), (1), and (2) to the single necessary equation for N_2, we have used the fact that levels (1) and (2) are thermalized by the phonon bath, so that $N_1 \simeq N_0\, e^{-E_1/kT}$ (where $E_1/kT \simeq 10$) and that $N_2 \ll N_0$, so that the ground state is only slightly depleted during lasing. All of the levels shown are actually crystal-field split manifolds, and

the cross sections σ^B and σ^A are the peak emission and absorption cross sections found from a population-weighted sum over transitions between different levels in each manifold. Both N_2 and βN_0 are spatially varying quantities, depending on the pump absorption parameters as described later. Defining the inversion density as $n \equiv N_2 - N_1(\sigma^A/\sigma^B)$, Eq. (21) becomes

$$\frac{dn}{dt} = -\frac{n}{\tau} - \frac{I}{I_s}\frac{n}{\tau} + \beta N - \frac{N}{\tau}\frac{\sigma^A}{\sigma^B} e^{-E_1/kT} \quad . \tag{22}$$

To remove the spatial dependence from the inversion n, we integrate over the laser mode volume. Here we use the approximation of a uniform laser mode intensity I and also neglect the longitudinal variation of I arising from spatial hole-burning effects. Defining

$$\mathfrak{n} \equiv \int_M n \, dV \quad ,$$

we have

$$\frac{d\mathfrak{n}}{dt} = -\frac{\mathfrak{n}}{\tau} - \frac{I}{I_s}\frac{\mathfrak{n}}{\tau} + \int_M \beta N dV - V_M \frac{N}{\tau}\frac{\sigma^A}{\sigma^B} e^{-E_1/kT} \tag{23}$$

where V_M = volume of laser mode in rod. We define the pumping rate by

$$R \equiv \int_M \beta N dV - V_M \frac{N}{\tau}\frac{\sigma^A}{\sigma^B} e^{-E_1/kT} \quad , \tag{24}$$

giving

$$\frac{d}{dt}\mathfrak{n} = \frac{1}{\tau_Q}\left(\frac{\tau_Q}{\tau}\right)\left[-\left(\frac{I}{I_s}\right)\mathfrak{n} - \mathfrak{n} + R\tau\right] \quad , \tag{25}$$

where we introduce the parameter τ_Q, the cavity lifetime, for later normalization purposes. In terms of other laser parameters, $\tau_Q = [2\mathfrak{L}/c(L + T)]$, where

$\mathfrak{L}$ = laser cavity optical length

c = speed of light

L = internal laser loss/round trip

T = output mirror transmission.

The next rate equation that is needed is for the saturable-absorber Q-switch in the laser cavity. In Fig. 11, taken from earlier studies on mini-laser rangefinders,[14] is shown a simplified energy-level diagram for the absorbing dye bis-(4-dimethylaminodithiobenzil)-nickel or the analogous ethyl complex, abbreviated as BDN.[15] The important parameters for the dye rate equation are σ_D, the absorption cross section from the singlet ground state, and τ_D, the decay time from the singlet excited state. There is absorption from the excited singlet S_1 state to the second excited singlet S_2, but since the nonradiative relaxation back to S_1 is so fast, the population of S_1 is presumed to be unaffected. The $S_1 \rightarrow S_2$ absorption with cross section σ_e will be included later as a loss term for the laser photons. With these approximations, the simplified

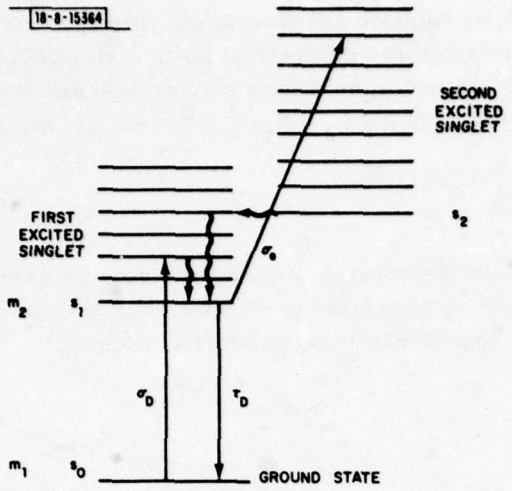

Fig. 11. Energy-level diagram for BDN dye, showing ground and excited-state cross sections, σ_D and σ_e, and excited-state decay time, τ_D. The absorptions indicated are at the lasing energy.

rate equations for the ground-state population density, m_1, and the first excited singlet density, m_2, are

$$\frac{dm_1}{dt} = -\frac{I}{h\nu}\sigma_D m_1 + \frac{m_2}{\tau_D}$$

$$\frac{dm_2}{dt} = \frac{I}{h\nu}\sigma_D m_1 - \frac{m_2}{\tau_D} \quad . \tag{26}$$

Note that $m_1 + m_2 = m_o$, the dye molecule density. In terms of the population difference, $m \equiv m_1 - m_2$, and the dye density m_o, $m_1 = (m_o + m)/2$ and $m_2 = (m_o - m)/2$, giving

$$\frac{dm}{dt} = -\frac{I\sigma_D}{h\nu}(m_o + m) + \frac{(m_o - m)}{\tau_D} \quad . \tag{27}$$

Normalizing the variables with respect to the dye density, saturation intensity, and cavity lifetime, Eq. (27) becomes

$$\frac{d}{dt}\left(\frac{m}{m_o}\right) = \frac{1}{\tau_Q}\left(\frac{\tau_Q}{\tau_D}\right)\left[-\frac{m}{m_o}\left(\frac{I}{I_s}\frac{\sigma_D\tau_D}{\sigma B\tau} + 1\right) - \frac{I}{I_s}\frac{\sigma_D\tau_D}{\sigma B\tau} + 1\right] \quad . \tag{28}$$

As a final check of Eq. (28), we note that in the steady state

$$\frac{m}{m_o} = \frac{1 - (I/I_s)(\sigma_D\tau_D/\sigma B\tau)}{1 + (I/I_s)(\sigma_D\tau_D/\sigma B\tau)} \quad , \tag{29}$$

in agreement with the steady-state populations calculated in Ref. 14.

The final variable for which we derive a rate equation is the laser mode intensity or, equivalently, the number of laser photons, q, within the cavity. If standing-wave effects are neglected, for a uniform laser mode of area A_m, $q = (I/I_s) A_m \ell/(c\sigma B\tau)$. Neglecting spontaneous emission into the laser mode, the photon number rate equation is

$$\frac{dq}{dt} = \left.\frac{dq}{dt}\right|_{\substack{\text{stimulated}\\\text{emission}}} + \left.\frac{dq}{dt}\right|_{\substack{\text{dye}\\\text{absorption}}} + \left.\frac{dq}{dt}\right|_{\substack{\text{cavity}\\\text{decay}}}$$

$$= -\int \left.\frac{dn}{dt}\right|_{\substack{\text{stimulated}\\\text{emission}}} dv + \int\left(\left.\frac{dm_1}{dt}\right|_{\text{absorption}} + \left.\frac{dm_2}{dt}\right|_{\text{absorption}}\right) dv - \frac{q}{\tau_Q}$$

$$= \frac{1}{\tau}\int\left(\frac{I}{I_s}\right) n\, dV - (\sigma_D m_1 + \sigma_e m_2)\frac{I}{h\nu} A_m \ell_D - \frac{q}{\tau_Q} \quad . \tag{30}$$

where

ℓ_D = Q-switch length

A_m = laser mode area .

Expressing q in terms of the normalized intensity gives

$$\frac{d}{dt}\left(\frac{I}{I_s}\right) = \frac{c\sigma^B}{A_m \ell}\left(\frac{I}{I_s}\right)\int_M n dV - \left(\frac{I}{I_s}\right)\frac{c}{\ell}\ell_D(\sigma_D m_1 + \sigma_e m_2) - \left(\frac{I}{I_s}\right)\frac{1}{\tau_Q}$$

$$= \frac{1}{\tau_Q}\left(\frac{I}{I_s}\right)\left[\frac{2\sigma^B}{A_m(L+T)}\pi - \frac{2(\sigma_D m_1 + \sigma_e m_2)\ell_D}{(L+T)} - 1\right] \quad . \tag{31}$$

In Eq. (31) we choose to normalize the integrated inversion by a parameter $\pi_T = A_m(L+T)/2\sigma^B$, which would be the threshold inversion in the absence of the saturable absorber. In terms of this parameter, we also define $R_T = \pi_T/\tau$, which is the threshold pump rate without dye loss. With these definitions, Eq. (25) becomes

$$\frac{d}{dt}\left(\frac{\pi}{\pi_T}\right) = \frac{1}{\tau_Q}\left(\frac{\tau_Q}{\tau}\right)\left[-\left(\frac{I}{I_s}\right)\frac{\pi}{\pi_T} - \frac{\pi}{\pi_T} + \frac{R}{R_T}\right] \quad , \tag{32}$$

and Eq. (31) becomes

$$\frac{d}{dt}\left(\frac{I}{I_s}\right) = \frac{1}{\tau_Q}\left(\frac{I}{I_s}\right)\left[\frac{\pi}{\pi_T} - \frac{2(\sigma_D m_1 + \sigma_e m_2)\ell_D}{(L+T)} - 1\right]$$

$$= \frac{1}{\tau_Q}\left(\frac{I}{I_s}\right)\left\{\left(\frac{\pi}{\pi_T}\right) - \frac{2m_o \ell_D \sigma_D}{(L+T)}\left[\left(\frac{m}{m_o}\right)\left(1 - \frac{\sigma_e}{\sigma_D}\right) + \left(1 + \frac{\sigma_e}{\sigma_D}\right)\right]\frac{1}{2} - 1\right\} \quad . \tag{33}$$

Next, we express time in terms of a dimensionless variable t/τ_Q, and define the normalized variables by

$\bar{\pi} \equiv \pi/\pi_T$

$\bar{I} \equiv I/I_s$

$\bar{m} \equiv m/m_o$

giving the final dimensionless rate equations:

(gain inversion) $\qquad \dot{\bar{\pi}} = \lambda[-\bar{I}\pi - \pi + \rho]$ (34)

(intensity) $$\dot{\bar{I}} = \bar{I}\bar{n} - \bar{I}[1 + \frac{\beta}{2}(1 + \epsilon)] - \bar{I}\bar{m}\frac{\beta}{2}(1 - \epsilon) \tag{35}$$

(dye population) $$\dot{\bar{m}} = r[-\bar{I}\gamma(\bar{m} + 1) - \bar{m} + 1] \quad , \tag{36}$$

where the dimensionless parameters are

$\lambda = \tau_Q/\tau$

$\rho = R/R_T$

$\beta = 2m_o \ell_D \sigma_D/(L + T)$ = ratio of unsaturated dye loss to cavity loss

$\epsilon = \sigma_e/\sigma_D$

$r = \tau_Q/\tau_D$

$\gamma = \sigma_D \tau_D/\sigma^B\tau$

and the dot superscript denotes differentiation with respect to the normalized time variable.

The final quantity which is necessary for solution of the rate equations is the normalized pumping parameter, ρ, which we now calculate using the lamp emission and rod absorption. The actual laser heads we have used have a close coupling geometry, with the lamp and square rod in close proximity, and both surrounded by an aluminized circular cross section reflector. This arrangement leads to a nonuniform and complex absorption profile, so for ease of calculations we have chosen to model the arrangement using a cylindrical rod with uniform illumination around the circumference. The intensity of the blackbody source at the rod surface is assumed to be

$$p_o(\lambda)\,d\lambda = \eta_L 2\pi h \frac{c^2}{\lambda^5} \frac{d\lambda}{e^{hc/\lambda kT} - 1} \tag{37}$$

where η_L is a lamp radiative efficiency factor. We will assume that the flux in the rod at each wavelength is exponentially decreasing as a function of the radius, so that the volume integrated pumping rate is found from integrating the spatially dependent power density divided by the pump photon energy, and multiplying by the absorption coefficient, $(\beta N)_\lambda = \alpha p_r(\lambda)/h\nu$, giving

$$\int dV\,\beta N = \int d\lambda \frac{8\pi^2 c}{\lambda^4} \frac{\ell}{\alpha} \frac{1}{e^{hc/\lambda kT} - 1} e^{-\alpha r_o}[\alpha r_M \sinh \alpha r_M - \cosh \alpha r_M + 1] \quad , \tag{38}$$

where

$\alpha(\lambda)$ = NPP absorption coefficient

r_o = laser rod radius

r_M = laser mode radius .

For generality we have allowed the rod and mode radii to be different, so that we may examine the effects of having incomplete filling of the rod volume by the laser mode. The absorption coefficient is an experimentally measured quantity. The electrical input energy to the flash

lamp appears implicitly in Eq. (38) through the blackbody temperature T. This temperature is found by equating the peak radiated power to the integrated spectral intensity,

$$P_{lamp} = \sigma T^4 \times 2\pi r_o \ell \quad , \tag{39}$$

where

σ = Stefan-Boltzmann constant = $5.67 \times 10^{-8} W/m^2K^4$

r_o = lamp discharge radius = laser rod radius

ℓ = lamp length = laser rod length ,

and then equating the integral of P_{lamp} times a normalized Gaussian time pulse to the electrical energy into the lamp. Finally, the resonant absorption term in Eq. (24) is subtracted from Eq. (38) to give the pumping rate R, which is then normalized by R_T. We have also included an attenuation factor of 0.5 to allow for the effects of pump collector absorption by the aluminum coating (about 10%) and for obscuration by the lamp itself and imperfect lamp imaging onto the rod. The coupled Eqs. (34)-(36) were solved numerically on an IBM 370/168 computer using a standard Runge-Kutta method. The solutions were carried out with the normalized values, and then scaled to the actual physical values using the input parameters such as pump energy, cavity loss, and saturable-absorber loss. Normal mode (non-Q-switched) laser behavior was found quite simply by setting the parameter $\beta = 0$.

Up to this point we have treated the Nd concentration as being a fixed parameter, $N = 3.9 \times 10^{21}$ cm^{-3} for pure NdP_5O_{14}. However it is possible to replace Nd by the optically inert rare-earth La to obtain $Nd_xLa_{1-x}P_5O_{14}$, so that one has control over some of the fluorescence properties of the laser material. The primary effects of varying the fractional Nd concentration, x, are threefold; (1) The absorption coefficients, approximately proportional to x, will change and give different spatial inversion and gain densities across the rod cross section. (2) The thermal population of the terminal $^4I_{11/2}$ manifold will vary with x, changing the resonant self-absorption loss and laser threshold. (3) The nonradiative concentration quenching of the Nd^{3+} fluorescence decreases at lower Nd concentration, thus increasing the fluorescent lifetime, τ, of the upper $^4F_{3/2}$ laser manifold as x decreases. All of these effects can be readily incorporated in the rate equations by making the following substitutions:

$$\alpha \rightarrow \alpha x$$

$$N \rightarrow Nx$$

$$\tau \rightarrow \tau_o/(1 + qx) \quad ,$$

where τ_o = 350 μsec and $q_o \simeq 1.69$, as determined from our own experimental data. Other numerical values which were used in the calculations are as follows:

ℓ = laser cavity length = 10 cm

r_o = rod and lamp radii = 0.075 cm

$\sigma^A e^{-E_1/kT}$ = effective resonant absorption cross section = 6×10^{-24} cm^2

σ^B = effective emission cross section = 1.5×10^{-19} cm^2

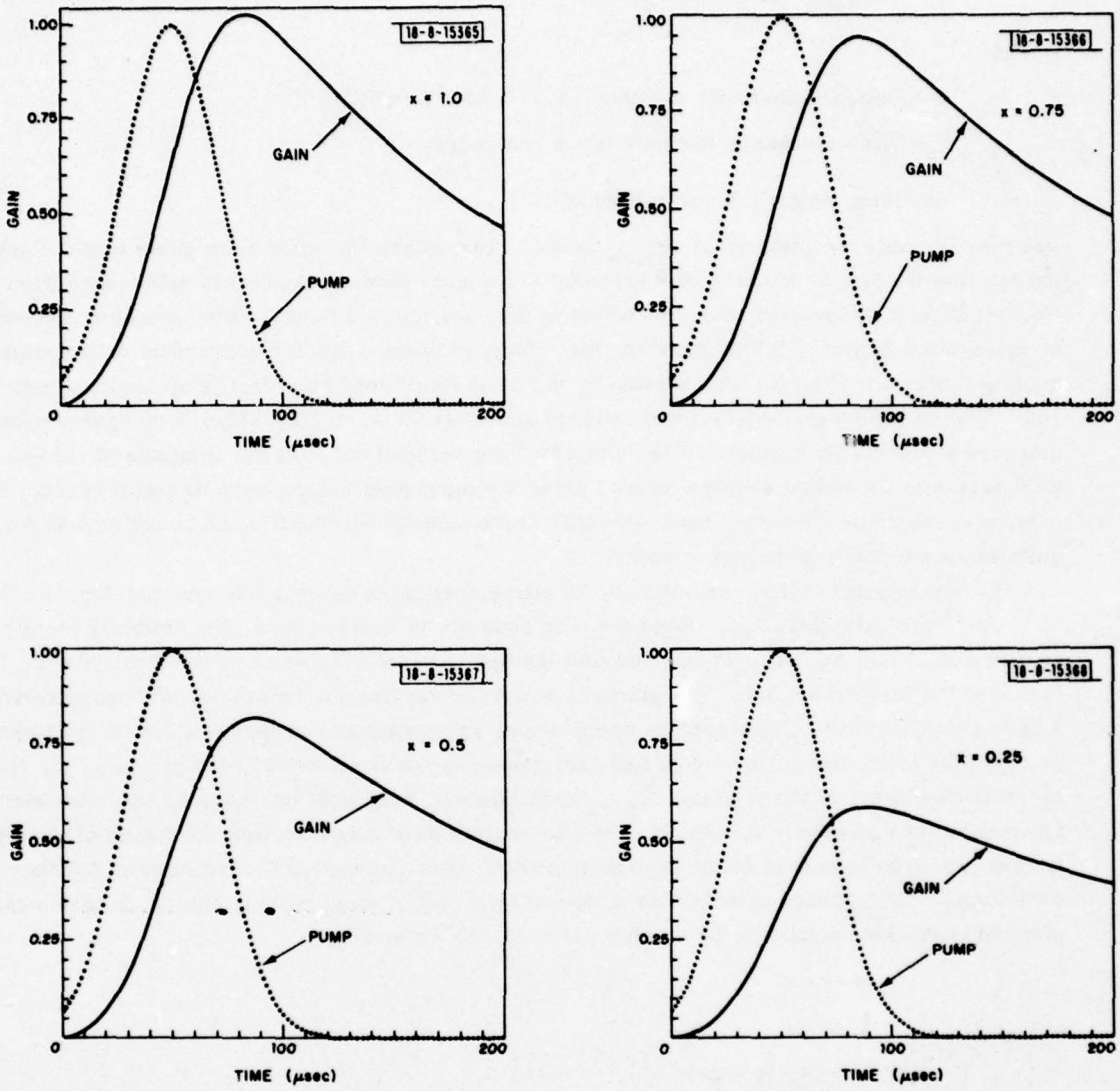

Figs. 12-15. Gain as a function of time for 1-cm-long NPP laser rod with flash-lamp pump having the indicated relative time dependence. Each gain curve is for a different fractional Nd concentration, ranging from x = 1.0 to x = 0.25.

σ_D = ground-state dye absorption cross section = 1.2×10^{-16} cm^2

σ_e = excited-state dye absorption cross section = 2.85×10^{-17} cm^2

τ_D = dye decay time = 1.87×10^{-9} sec .

The input variables for each calculation were the excitation energy, Nd concentration, cavity loss (assumed to be entirely from the output coupler), unsaturated dye loss, and mode area.

3. Absorption and Gain Characteristics

Before giving the calculated laser results, we examine some of the absorption and gain characteristics. In Figs. 12 to 15 is shown the gain $2g\ell$ as a function of time for 1 J pump energy in lasers with different Nd concentration x = 1.0, 0.75, 0.50, 0.25. The gain parameter plotted on the vertical axis is the round-trip gain of the uniform laser mode through the 1-cm-long laser rod, and is found by integrating the spatially nonuniform inversion over the rod cross section. As expected, the gain decreases with lower absorption and the peak of the gain shifts slightly to longer times as the fluorescence lifetime increases. However, for the relatively short pump pulse being used (with normalized time dependence given by the dashed curves), the pump is absorbed in a time small compared with decay or quenching times for any concentration. Therefore, even though the fluorescence decay characteristics for times greater than 100 μsec can be seen to differ with different values of x, the gains for shorter intervals do not depend on τ directly, but rather on the pump absorption strength and to some extent, on the resonant absorption loss. Clearly this will not be the case for CW lasers, where τ plays a direct and significant role in determining the steady-state inversion and gain. Another interesting point seen in these curves is that the peak of the gain occurs 30 to 40 μsec after the peak of the pump pulse, so that an optimally designed Q-switched laser should hold off lasing until this maximum energy storage condition is reached in order to extract the most energy in a single short pulse.

The spatial dependence of the pumping found from the absorption spectrum of NPP and the blackbody lamp emission is shown in Fig. 16, for a 1-J pump energy and the four previous Nd concentrations. Because of the large peak absorption coefficients in NPP, the strongest concentration dependence on the inversion appears near the surface of the laser rod. In the interior, the inversion is more insensitive to concentration because the weaker peak absorptions of the dilute (Nd, La)PP give absorption strengths comparable with those arising from the wings of the absorption distribution in NPP. For the uniform laser mode the differential inversion, rn(r), is plotted in Fig. 17, and shows the relative contribution to the mode gain from the inversion at a distance r from the rod center.

4. Normal-Mode Laser Output

Next, a typical laser output pulse is shown in Fig. 18, in this case with x = 1.0 and 1 J pump energy into the lamp. We have taken the output mirror transmission (representing the entire cavity loss) equal to 0.2 and have not included any dye loss. The oscillatory output comes from the relaxation oscillations induced by the rapid population inversion and overshoot from the equilibrium threshold level. Such oscillations are commonly observed in solid-state lasers, particularly those having long fluorescent lifetimes. In our case, the regularity of the oscillation comes from our assumption of a single-mode output. In actual practice, multi-longitudinal

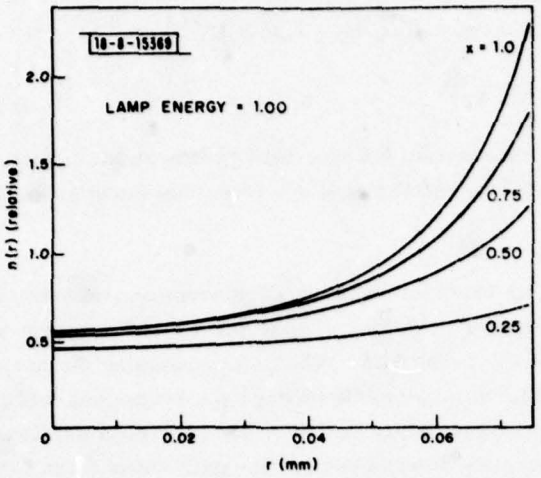

Fig. 16. Inversion density n(r) as a function of radial coordinate in a 1.5-mm-dia. (Nd, La) PP rod with 1 J pump energy for the different fractional Nd concentrations indicated.

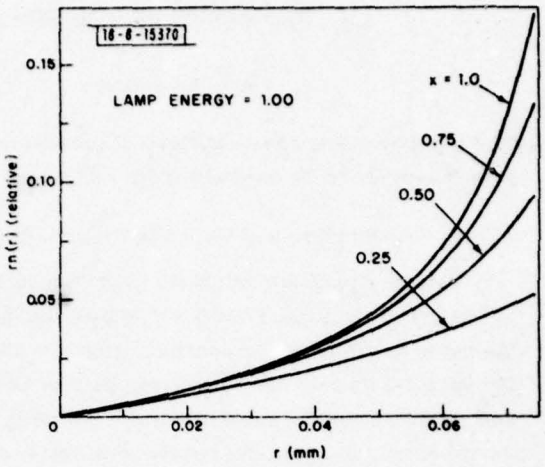

Fig. 17. Differential inversion density rn(r) as a function of radial coordinate in a 1.5-mm-dia. (Nd, La) PP rod with 1 J pump energy for the different fractional Nd concentrations indicated.

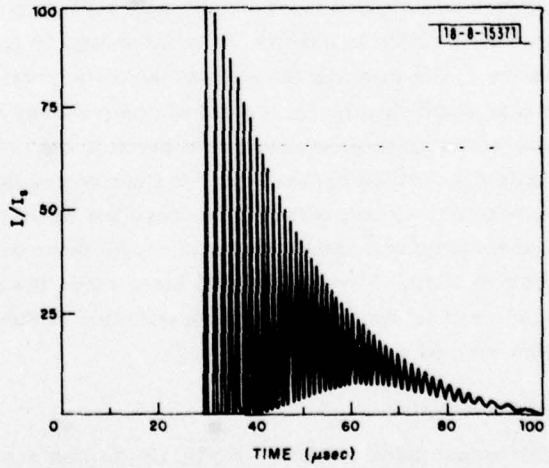

Fig. 18. Calculated normalized output intensity I/I_s as a function of time for a 1.5-mm-dia., 1-cm-long NPP rod with 1 J energy input and 20 percent output mirror transmission. The integrated absolute output energy is 24 mJ.

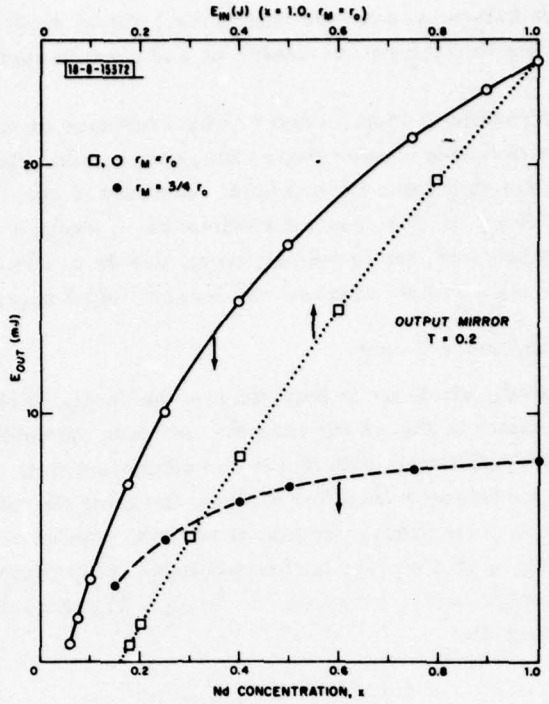

Fig. 19. Calculated output energy as a function of input energy (dotted curve, top scale) for the NPP laser with complete mode filling of the rod ($r_M = r_o$). Output energy as a function of Nd concentration x with 1 J energy input, and $r_M = r_o$ (solid curve, bottom scale) and $r_M = 3/4\ r_o$ (dashed curve, bottom scale).

and transverse modes cause a highly irregular spiking. In any case, we are not concerned so much with the detailed time behavior of the normal-mode output, but rather its time integral, which gives the output pulse energy. In this case, we have an output energy of 24 mJ, with 1 J input.

Curves and data for normal-mode operation similar to Fig. 18 were calculated varying several parameters and these are summarized in Fig. 19. First, as a check on the validity of the calculations, we computed a curve of output vs input energies (dotted curve, top horizontal axis). Both the threshold and peak output energy are in good qualitative agreement with experimental results to be discussed in the next section. The slight deviation from linearity probably stems from the conversion of input energy to blackbody lamp temperature, with a consequent lowering of the emission peak from 0.54 μm at ~0.2 J input, to 0.36 μm at 1 J input. Such a shift in the emission spectrum away from the Nd^{3+} absorption regions would cause a nonlinear decrease in absorption efficiency. Next, to compute the optimum Nd concentration for maximum energy output we calculated E_{out} as a function of concentration x (lower horizontal axis) for a fixed input energy of 1 J (solid curve). As might be expected from the earlier gain calculations, the maximum concentration x = 1.0 gives the best absorption and the most output energy, with the smaller effects of larger concentration quenching and resonant loss not being significant. The calculations for the very lowest concentrations ($x \lesssim 0.3$) are probably not as accurate as the

high-concentration values because our laser model did not include reabsorption of pump radiation partially transmitted through the laser rod and re-reflected by the pump collector back into the rod.

In view of the results of Figs. 16 and 17 which indicate nonuniform absorption, we have calculated the effects of having a laser mode which does not completely fill the rod, as might be caused by edge diffraction loss, for example. The dashed curve in Fig. 19 shows the calculated result for $r_M = 0.75\ r_o$, in this case a 1.13-mm-dia. mode in a 1.5-mm-dia. rod. The maximum output decreases from the previously mentioned 24 to 8 mJ. Even though the concentration dependence is significantly reduced, the largest output energy is still obtained for x = 1.

5. Q-Switched Laser Output

When the saturable absorber is inserted into the cavity, lasing oscillation is suppressed until the gain, as shown in Fig. 12 for example, exceeds the combined cavity and unsaturated dye loss. The laser oscillation then builds up rapidly in a time on the order of τ_Q, and as it does, the laser mode intensity bleaches the dye, lowering the total loss, and increases the mode buildup still further. This process continues until the population inversion is depleted and the mode decays, resulting in a single short output pulse if the pump and loss parameters are properly chosen. If the dye loss is too large, no lasing will occur, and if it is too small, multiple output pulses may result.

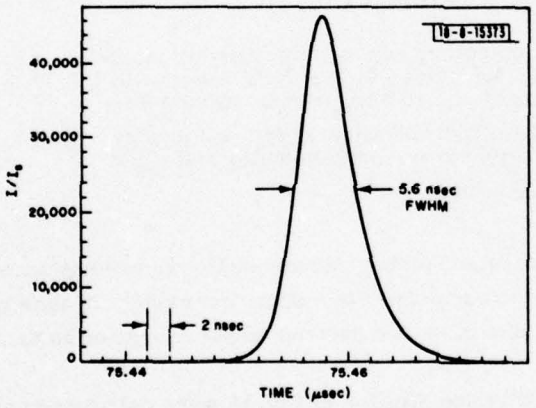

Fig. 20. Calculated Q-switched output intensity as a function of time for NPP rod with 1 J input. The output coupling is 0.2, the unsaturated dye absorption is 0.8, and the integrated energy is 10.2 mJ.

A typical Q-switched output pulse for 1 J input and x = 1 is shown in Fig. 20. The output mirror transmission is 0.2 and the unsaturated dye loss is 0.8, near the maximum allowed for 1 J input. The time scale is shown greatly expanded compared with Fig. 18, and only a small portion containing the single output pulse ~75 μsec after the start of the pump is shown.

All parameters were held fixed (E_{IN} = 1 J, x = 1.0) except for mirror transmission and unsaturated dye loss, and the resulting Q-switched output behavior is summarized in Fig. 21. First, with the output mirror transmission held at T = 0.2, the Q-switch loss was varied from 0.45 to 0.8, approximately the range between threshold ($T \gtrsim 0.85$) and double-pulsing ($T \lesssim 0.4$). The output energy (open circles, dashed curve, left scale) increased monotonically from 7.8 to 10.2 mJ, and the pulse width (full-width, half-maximum) decreased monotonically from 9.0 to 5.6 nsec (open circles, solid curve, right scale). These results showed that at 1 J input, the maximum total loss was 1.0, so this parameter was fixed and both the Q-switch loss and mirror

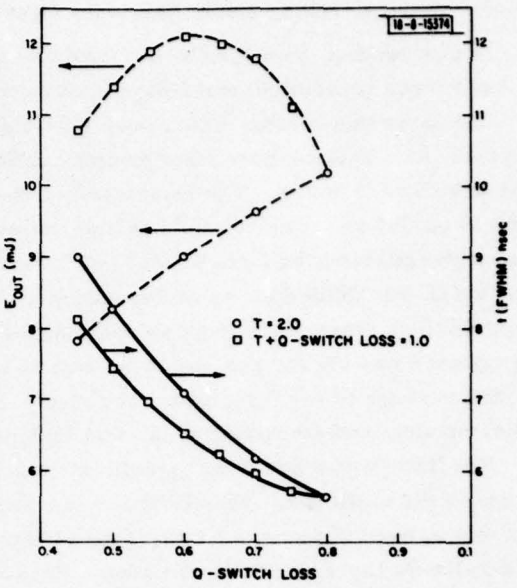

Fig. 21. Calculated Q-switched energy output (left scale, dashed curves) and full-width, half-maximum pulse duration (right scale, solid curves) as a function of Q-switch loss. The curves connecting the circles refer to fixed output mirror coupling of 0.2, and the curves connecting the squares refer to variable coupling, maintaining the total coupling plus Q-switch loss at 1.0.

transmission were varied, but maintaining the sum constant at 1.0. This procedure showed that the maximum theoretical energy extraction occurred for the optimum combination of T = 0.4 and Q-loss = 0.6, with an energy output of 12.1 mJ and a pulse width of 6.5 nsec. The maximum in the power dependence is a weak one, but it would be better to choose that operating point primarily for the most stable laser output, midway between the threshold and double-pulsing conditions.

B. EXPERIMENTAL STUDIES

1. Overview

The experimental studies of NPP lasers that we have undertaken are a continuation of our original work using flash-lamp excitation, which was previously reported.[4] The main effort was to increase the output energy and efficiency of the laser, to study its Q-switched behavior and maximize the short-pulse output energy, and in so far as possible, provide experimental evidence to give confidence in our numerical simulation, described above.

One of the laser parameters which we had varied in the computer calculations and which we hoped to study experimentally as well was the Nd concentration in the laser rod. Although we expect that pure NPP will have the best absorption efficiency, other factors such as the laser mode nonuniformity and the details of the absorption profile in the square rod make the laser output calculations somewhat imprecise. Clearly, it would be desirable to have rods of (Nd, La) PP to study such effects and compare with the calculations of Fig. 19. Unfortunately, as La replaces Nd, large high-quality pentaphosphate crystals become more difficult to grow. The main problem seems to arise from strains in the mixed crystals which make it nearly impossible, at the present time, to cut and polish laser rods without introducing cleavage cracks. Although further studies of the growth process may improve this situation, because of the unavailability of the dilute rods, all of the experimental results described in this report were obtained with pure NdP_5O_{14} laser rods.

2. Normal-Mode, Stable Resonator Operation

In this section, we describe the experimental results using a stable confocal resonator (with 10 cm mirror separation) and normal-mode (non-Q-switched) operation.

The laser parameters which were investigated under these conditions were the effects of rod size, end facet coatings, and pumping uniformity. The basic laser system was similar to that described in Ref. 4. The laser cavity consisted of dielectric-coated mirrors with 10-cm radii of curvature. One mirror had high reflectivity (>99.9%) at 1.05 μm, and different end mirrors with reflectivities from 97.5% to 80% were used. The laser head consisted of an aluminum body which was drilled out to accommodate a 6-mm-i.d. glass tube, whose inner surface was aluminized by evaporation from an aluminum-wetted tungsten filament. One edge of the reflecting cylinder was slotted parallel to its axis to allow insertion of a metal tab to which was cemented the edge of the laser rod. The side of the aluminum body was also slotted next to the reflector slot, and the mounting tab was clamped by the aluminum body.

The flash lamps had hard borosilicate glass envelopes, with a 1.5-mm i.d., and a high-pressure fill of Xe gas. The electrode separation was varied to match the length of the laser rod, but in most cases was 1 cm. These lamps are an experimental type, supplied to us by the GTE Sylvania Lighting Products Group. Because the fabrication procedure was newly developed, no precise control or knowledge of the fill pressure was available, but it was estimated to be approximately 1500 Torr.

The lamp was inserted in the pump reflector assembly parallel with and immediately adjacent to, but not contacting, the laser rod. It was mounted by cementing the glass envelope to plastic end pieces attached to the ends of the aluminum reflector body. Bayonet-type connector pins were soldered via flexible copper sheet leads to the lamp electrodes. The lamp was fired through a standard LC discharge network. We used a 10-uF (2 kV rated) storage capacitor with a 60-μH coil inductance. The lamp trigger voltage was supplied through a series trigger transformer unit (EGG type TM-12A), which added a small, saturating inductance to the circuit. The current waveform was a smooth, bell-shaped curve with about a 50-μsec FWHM duration, and peak current (at 1 J) of about 120 A. The repetition rate was set with a low-frequency function generator, which in turn triggered another pulse generator with pulse-delay capability, shorter pulses, and higher output voltages. This narrow-pulse output triggered the EGG high-voltage trigger module, discharging the 10-uF capacitor which had been charged with a standard variable-voltage DC supply through a 30-kΩ current-limiting resistor.

The laser output pulses were measured with a Si photodiode terminated by 50 Ω (for fast response) at the oscilloscope input. Integrated pulse energies were measured by a Scientech 362 thermopile meter, and generally obtained from an average of several laser shots, i.e., measuring the total energy of about ten successive shots and dividing by the number of shots. For examination of the laser transverse mode distribution, a flip-in mirror diverted the laser beam onto an opaque screen, at the focus of an infrared-sensitive TV camera whose picture was displayed on a TV monitor.

First, we shall review the results obtained with rods of different sizes. All rods described below had the "c" axes parallel to the lasing direction, and had polished end faces. The most significant improvement over the initial results[4] obtained with the same size rod came from four factors: (1) adjusting the end mirrors for multimode output in order to fill the rod volume, (2) using high-pressure Xe lamps for more efficient operation, (3) using a slightly more closely

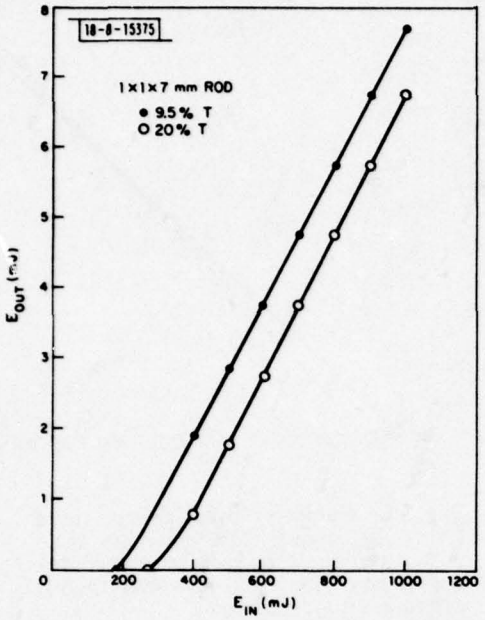

Fig. 22. Output vs input energy for a 1- × 1- × 7-mm NPP rod in a 10-cm confocal cavity with 9.5% and 20% transmitting output mirrors.

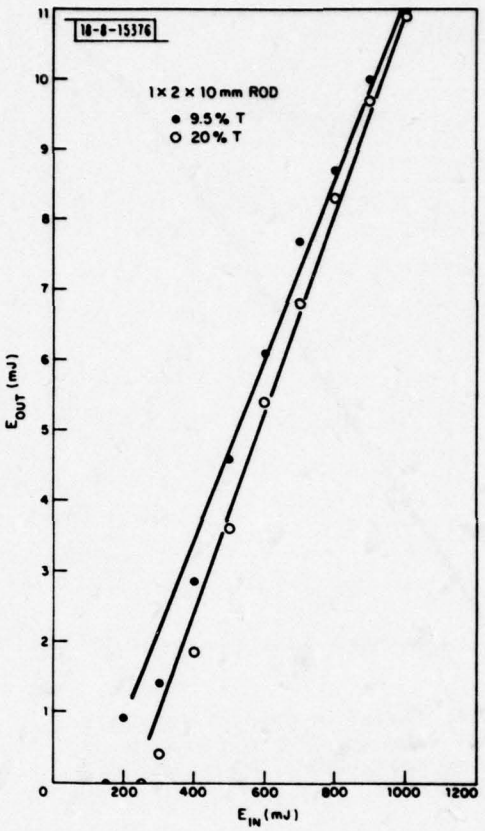

Fig. 23. Output vs input energy for a 1- × 2- × 10-mm NPP rod in a 10-cm confocal cavity with 9.5% and 20% transmitting output mirrors.

coupled pump collector, and (4) lowering the repetition rate to 12 pulses per minute (0.2 Hz) to eliminate rod heating effects and ensure full charging of the lamp capacitor. With these improvements, we have obtained laser outputs shown in Fig. 22, using a 1- × 1- × 7-mm rod and two different output mirrors of 9.5% and 20% transmission. In this case, the slope efficiencies, ~1 percent, are nearly the same, implying that the internal laser losses are much less than 10 percent.

Figure 23 shows the results using a 1- × 2- × 10-mm rod, with the broad 2- × 10-mm face adjacent to the flash lamp. The maximum output energy at 1 J input has increased nearly 40 percent to 11 mJ, and the slope efficiency for the 20% T mirror has increased to ~1.4 percent. Again the most significant difference between the results with the two output couplers is the increased threshold with increasing mirror transmission, although here there is also a slight but noticeable increase in slope efficiency as well.

In order to obtain more energy from the NPP laser, the next step was to increase the length of both the rod and lamp. This was done primarily in order to drive the lamp to higher levels without shortening its life. The lamp explosion energy for the glass, high-pressure lamps is not known, but the value for quartz, low-pressure (450 Torr) lamps is estimated from various manufacturers' literature[16] to be on the order of 20 J/cm for our present pulse width. The

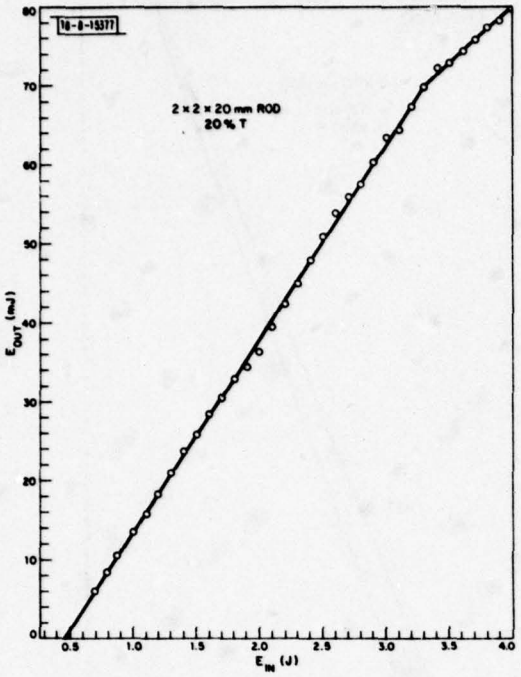

Fig. 24. Output vs input energy for a 2- × 2- × 20-mm NPP rod in a 10-cm confocal cavity with a 20% transmitting output mirror.

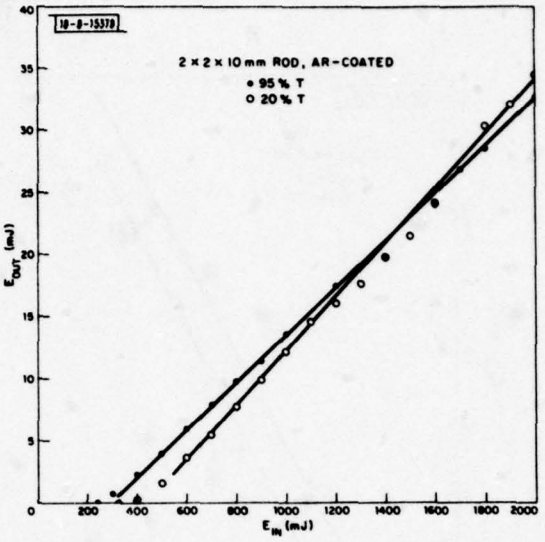

Fig. 25. Output vs input energy for a 2- × 2- × 10-mm NPP rod with anti-reflection coatings in a 10-cm confocal cavity with 9.5% and 20% transmitting output mirrors.

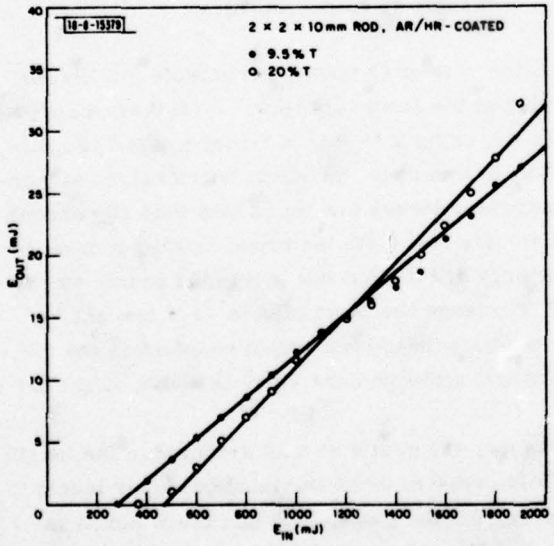

Fig. 26. Output vs input energy for a 2- × 2- × 10-mm NPP rod with one end having a high-reflection coating and the other an anti-reflection coating. The semiconfocal cavity was 5 cm long with 9.5% and 20% transmitting output mirrors.

lamp lifetime (number of flashes) should increase nearly exponentially with decreasing operating energy, expressed as a percentage of the explosion energy. In our case, the factors of a higher pressure fill and a less durable envelope would probably decrease the explosion energy, possibly to ~10 J/cm. Therefore, we estimate that for a lamp input of 4 J, the life of a longer lamp would be extended from $\sim 10^3$ to 10^4 flashes to $>10^5$ flashes. Another benefit would be to lower the peak current density and color temperature, shifting the blackbody emission peak towards the Nd^{3+} absorption bands. Using a larger rod cross section of 2 × 2 mm and the previous lamp diameter, but increasing both rod and lamp to 2 cm length gives the results shown in Fig. 24 with a 20% T output mirror. In this case, the longer lamp led to unreliable firing below ~350 V, so that the laser threshold and lowest level outputs were not measured. Extrapolating from the data, the estimated threshold is ~400 mJ. The output remains linear up to input energies near 3.4 J, with a slope efficiency of 2.5 percent. In this regime, we obtain a maximum energy of 72 mJ with 3.4 J input, for a 2.1-percent total efficiency. Beyond this energy, the slope efficiency decreases markedly to 1.3 percent, and the maximum output at 4 J is 80 mJ, whereas the output with continued 2.5-percent slope efficiency would be 88 mJ. The most probable cause for the decrease in efficiency is related to the onset of oscillating modes not requiring the 80%-reflecting output mirror. We observed that with removal of the output mirror, lasing occurred at a threshold near 3.2 J. This means that sufficient gain had built up to allow oscillation with the high-reflecting end mirror and the 5% reflectivity of the uncoated NPP rod facet. The near-field output of this mode was a narrow stripe with orientation parallel to the pumped face of the laser rod, indicating that sufficient gain for this mode occurred only near the pumped surface. Using the high-gain approximation, with the threshold condition $\exp(2gl) = 1/R$, gives the gain coefficient $g \sim 0.75\ cm^{-1}$.

In all of the results given so far, the ends have been polished but not coated. In order to see if these uncoated faces were causing any significant losses in the laser, we have measured the laser output using a rod with dielectric anti-reflection coatings on the ends. A 1- × 2- × 10-mm AR-coated rod was tested in the confocal cavity with the 20% T output mirror. The threshold was 250 mJ, and the output at 1 J input was 10.1 mJ. These results are nearly identical with those found using the uncoated 1- × 2- × 10-mm rod (Fig. 23) with threshold of 250 mJ and output of 10.9 mJ.

The results with a 2- × 2- × 10-mm AR-coated rod are shown in Fig. 25. Both the overall and slope efficiencies are somewhat larger than in the case of the 1- × 1- × 10-mm rods. The 9.5% T and 20% T mirrors give slope efficiencies of 1.9 and 2.2 percent, respectively. As seen in Fig. 25, the maximum output energy is 34.5 mJ with 2 J input energy. Over some of the range of input energy, there seems to be a systematic deviation from the linear output vs input characteristic, but it is not known whether this is associated with the lamp behavior or the laser-rod absorption.

Next, a similar 2- × 2- × 10-mm rod was tested with one face AR-coated as before, and the other face coated with a high-reflectance dielectric coating to compare such an end reflector with the external, 10-cm-radius HR mirror. The external HR end mirror was removed, leaving a semiconfocal cavity with ~5 cm separation between the HR-coated rod face and the external output mirror. From symmetry considerations, the modes of this semiconfocal cavity should not differ significantly from those of the longer confocal cavity. The output vs input energy data for this laser are shown in Fig. 26, and differ little from those of the 2- × 2- × 10-mm AR rod with two external reflectors (Fig. 25).

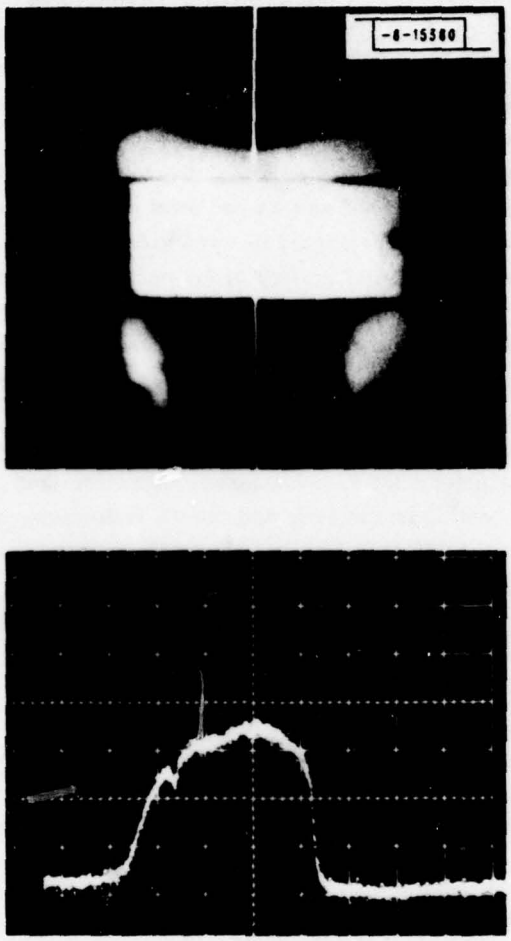

Fig. 27. Back-illuminated view of 1- × 2- × 10-mm NPP laser rod with mounting tab below and lamp above. The video analyzer signal from top to bottom along the white scan line is shown below the laser rod view with signal intensity proportional to brightness.

A comparison of the experimental results with the previous normal-mode calculations is best made using the data of Fig. 23 for the 1- × 2- × 10-mm rod. This area of 2 mm^2 is close to the cylindrical area of 1.77 mm^2 for the 1.5-mm-dia. rod assumed in the numerical analysis. With the 20% T output mirror, the experimental and theoretical thresholds are 250 and 160 mJ, respectively, with output energies of 11 and 24 mJ at 1 J input. Considering the ab initio nature of the calculation, the agreement to within a factor of 2 is quite good. The uncertainty in the gain distribution within the rectangular rod, and in the exact mode profile can easily account for this difference, as demonstrated by the reduction of the calculated output from 24 to 8 mJ with a mode three-quarters the original diameter. Similarly, an overall reduction in the theoretical effective pumping efficiency by a factor of 2 would raise the threshold to ~300 mJ and lower the output to 12 mJ, giving excellent agreement with the experimental data. From these results, we conclude that the numerical simulation is an accurate semi-quantitative model which should be capable of predicting the concentration dependence of (Nd, La) PP laser rods, and of modeling the Q-switched behavior, described later.

Measurements were performed to determine the degree of pumping nonuniformity in the laser rod. The laser cavity mirrors were removed, the head rotated 90° about the rod axis, and the front surface of the laser rod was imaged directly onto the infrared-sensitive vidicon tube. A CVI 321 Video Analyzer was inserted between the camera control unit and the monitor, and provided a signal proportional to the picture intensity along a scan line perpendicular to the monitor raster scan. Figure 27 shows a photograph of monitor screen on which is seen the face of the 1- × 2-mm laser rod, with the mounting tab below it, and a circular edge of the pump lamp above it. This picture was obtained with tungsten lamp illumination of a card placed behind the laser rod. The vertical white line shows the scan axis for the video analyzer. Also shown in Fig. 27 is the oscilloscope display of the analyzer voltage along the scan line and is provided for calibration purposes. The right side of the oscilloscope trace shows the sharp drop in intensity between the laser rod and dark mounting tab (bottom part of scan), and the left side of the scan shows a narrow dip corresponding to the top edge of the rod adjacent to the lamp. After obtaining these photographs, the back illumination was removed, and with attenuators and visible-blocking, infrared-transmitting filters (Corning 2-64, 7-56) inserted, the Nd^{3+} fluorescence emission during the flash-lamp excitation was observed. Figure 28 (top) shows a photograph of the monitor displaying the fluorescence across the rod, and two scans (bottom) of that fluorescence pattern in the vertical direction with the right photograph showing a center scan, and the left photograph showing a scan near the left-hand edge of the rod. As is evident from Fig. 28, there is considerable nonuniformity of the pump absorption, particularly along the lamp-rod dimension where the absorption decreases by a factor of 2 across the 1-mm rod thickness. (The multiple scan traces in Fig. 28 are present because of the lack of synchronization between lamp firing and monitor scan, which necessitated photographing several analyzer scans.)

An attempt was made to improve the pumping uniformity of the NPP rod by constructing a dual-lamp (DL) laser head. A cross section comparing the single and DL configurations is shown in Fig. 29. As seen from the sectional view of the DL collector, the degree of coupling for each lamp was less than that in the single-lamp collector. Although the copper rod mounting tabs for the DL laser were polished and aluminized, we expect that light from the lamps entering the corners between the tabs and the glass sleeve was not efficiently reflected to the laser rod. The lamps in this unit were connected in series to insure full discharge current through both lamps. The procedure which we followed to examine the effects of pumping uniformity was to

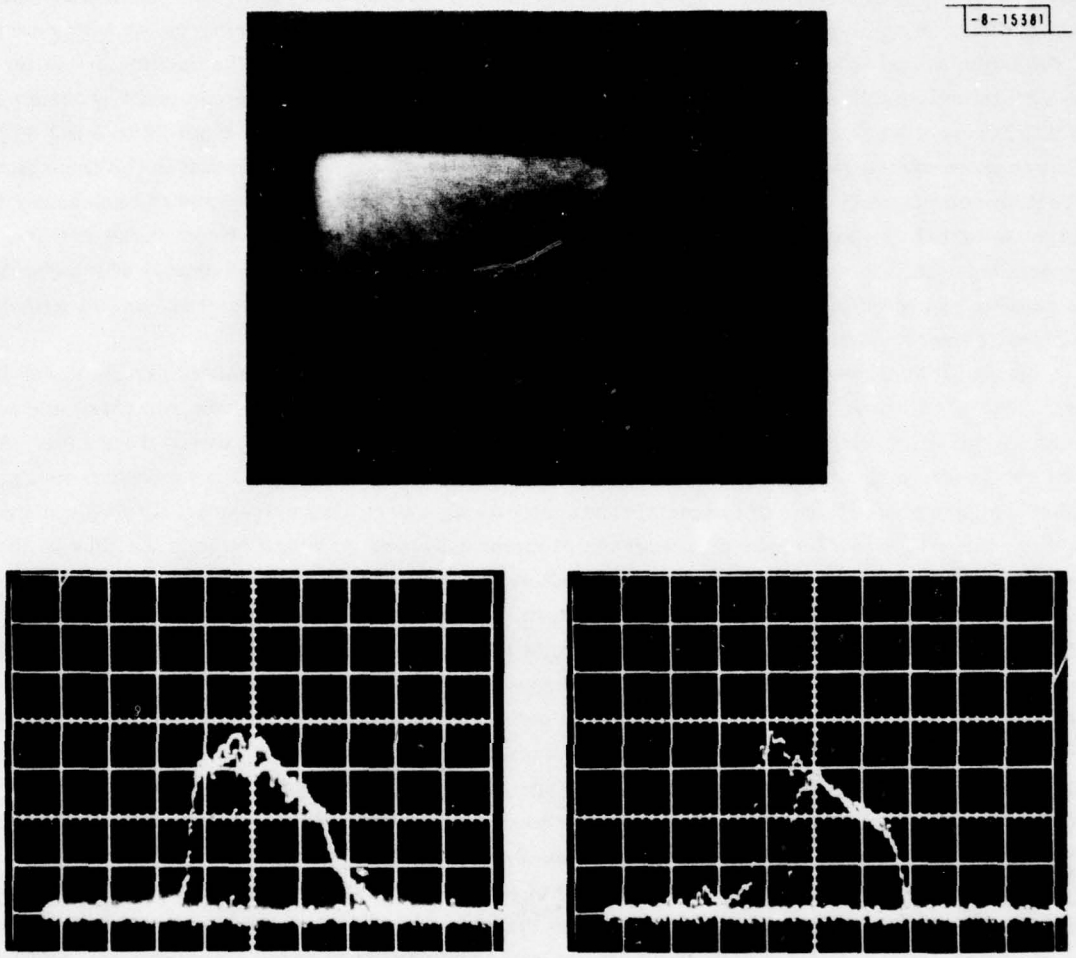

Fig. 28. Fluoresence emission from end face of NPP laser rod (top) and video analyzer scans along vertical lines (bottom). The left bottom trace is a scan near the left edge of the rod view, and the right bottom trace shows a scan at the rod center.

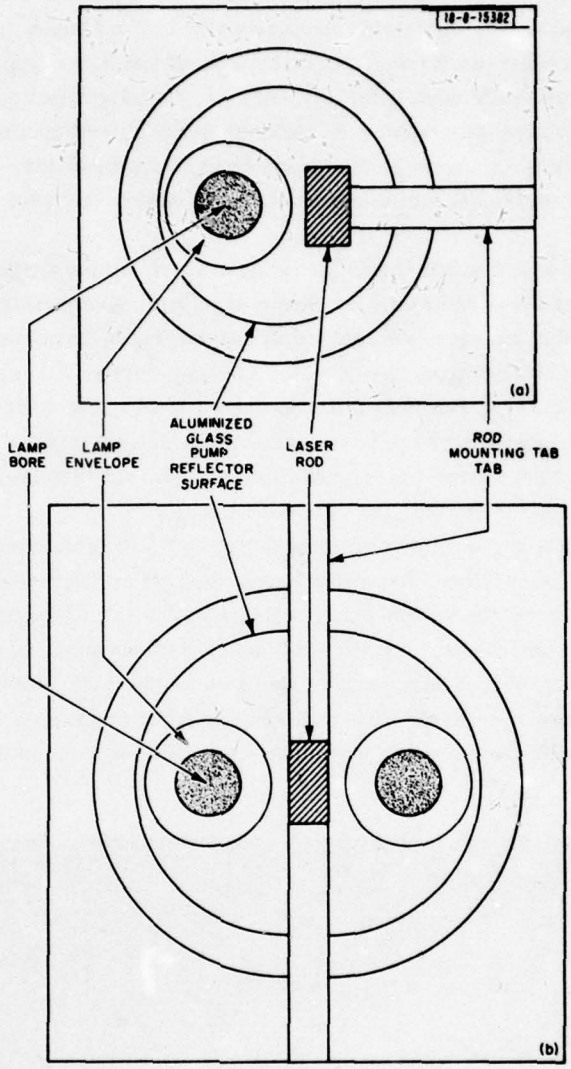

Fig. 29. Cross-sectional views of single-lamp (top) and dual-lamp (bottom) laser heads.

compare the laser output with each lamp fired individually with that when both lamps were fired, maintaining the same energy input. Firing both lamps gave an output of 19.2 mJ at 3 J input and 12.5 mJ at 2 J input. The threshold was below the minimum firing level for both lamps in series, 470 V or 1.1 J. Using the 2-J level for reference, one lamp gave an output of 7.8 mJ, and the other gave 2.3 mJ. Repeating the dual-lamp measurement at 1.6 J input then showed a decreased output of 4.9 mJ from the previous 9.1 mJ. Disassembly of the laser head showed that the rod had loosened from one of the side tabs, possibly affecting the alignment during the test. Also, slight crazing on the lamp bore was observed, although probably not enough to significantly alter the light output. It is possible that the second lamp is indeed poorer than the first, but we have not had the time to characterize all the lamps used, or to repair the head assembly and repeat the measurements.

Another modification of the single-lamp laser head which we investigated was the replacement of the aluminized reflector sleeve by a coating of high-diffuse-reflectance $BaSO_4$ paint (Kodak 6080) directly on the machined and etched aluminum laser head assembly. Using the 2- × 2- × 10-mm AR-coated laser rod, we obtained 25 mJ output at 2 J input, compared with the earlier result of 34.5 mJ. A different lamp was used in this test with a significantly higher discharge voltage, so the lamp may have contributed to the lower output. In view of the fairly good laser output and the simplicity of laser head fabrication, this spray-painted coating may be a practical alternative to the coated glass sleeve reflector.

In order to demonstrate the miniaturization possible with the flash-lamp-excited NPP laser, we have constructed a self-contained, hand-held laser unit. For increased ruggedness and miniaturization, we have replaced the hollow pump collector by a solid integral assembly. This consists of a 1-cm-long × 6-mm-dia. sapphire cylinder, with a round hole to accommodate the 2.5-mm-dia. Xe flash lamp and a 1-mm-square slot to hold the NPP laser rod, both of which are mounted using polystyrene cement. The outer surfaces of the sapphire collector were aluminized and overcoated with silicon oxide for protection. These components are shown in Fig. 30.

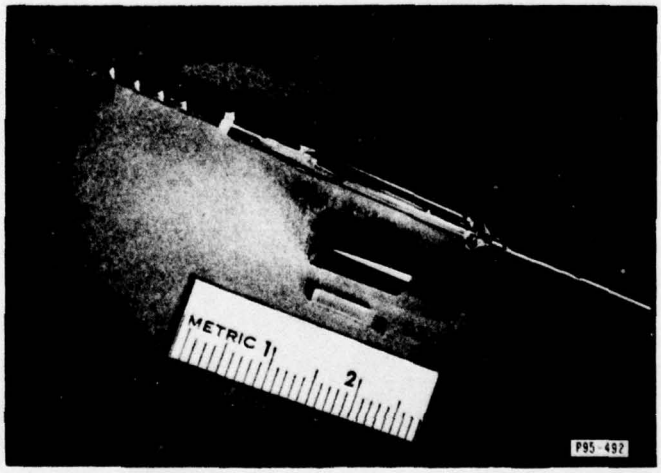

Fig. 30. Laser head components for hand-held laser, showing (from top to bottom) Xe flash lamp, sapphire pump collector, and NPP rod.

The laser head was mounted in a Vespel holder to which were attached the 1/2-in.-dia. laser mirrors, using adjustable O-ring mounts. The present laser has a semiconfocal cavity with a 13-cm-radius high-reflecting mirror and a flat, 10% transmitting output mirror.

The laser-cavity assembly is mounted on top of a power supply (2-1/2 × 3 × 5-3/4 in.) containing a commercially purchased DC inverter with LC pulse-forming network and SCR trigger circuitry. The inverter is powered by rechargeable 12-V Ni-Cd batteries, also mounted in the power supply, capable of providing one thousand 1-J discharges into the lamp. The laser is fired manually by a push-button switch at rates up to 1 Hz. The complete laser is shown in Fig. 31.

Fig. 31. Complete hand-held NPP laser with cylindrical laser cavity mounted on top of power supply.

The laser rod presently in use is 1/2 × 1 × 7 mm. The internal lamp and rod-mounting surfaces on the sapphire collector have a ground finish, which we have not index-matched to the lamp and rod. Because of these factors, we are presently limited to 0.5 mJ output with 1 J input. Using a 1-mm^2 rod and better cementing techniques, we should be able to achieve output energies comparable with the 10-mJ level (at 1 J input) obtained with our laboratory-bench hollow-collector laser heads.

The size of the present resonator assembly is determined primarily by the external mirrors and mounts. Using miniature mirrors fastened directly to the sapphire holder, or suitably polishing and coating the laser-rod surfaces themselves, would result in a much smaller laser assembly. Significant reduction in the power-supply size should also be achievable.

3. Q-Switched Operation, Stable and Unstable Resonators

The next phase of experimental study dealt with Q-switched operation of the NPP lasers using an intracavity saturable absorber. We used the dye bis-(4-diethylaminodithiobenzil)-nickel (Kodak 14617) having a molecular weight of 685.68. In most of the measurements, the dye was dissolved in toluene and the dye solution was held in specially fabricated cells inside the laser cavity. This was done primarily for the convenience of being able to vary the dye concentration and quickly change the Q-switch loss.

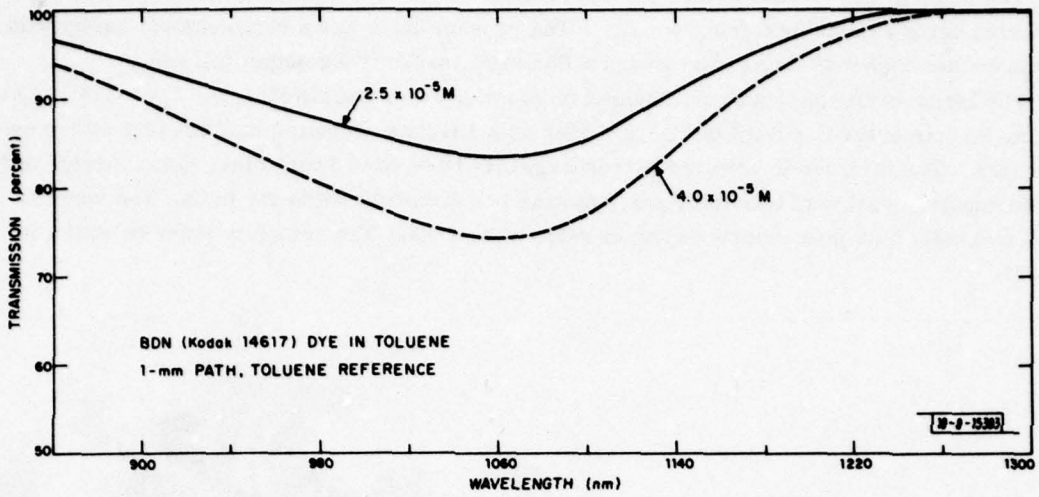

Fig. 32. Spectrophotometer absorption curves of transmission vs wavelength for 2.5×10^{-5} M (solid curve) and 4.0×10^{-5} M (dashed curve) solutions of BDN dye in toluene. The path length is 1 mm and a 1-mm cell of toluene was used as a reference.

A starting 1×10^{-4} M solution of dye was prepared by dissolving 14.37 mg of dye powder (2.1×10^{-5} moles) in 210 ml of toluene, and lower concentration solutions were then made by appropriate dilution. Figure 32 shows two spectrophotometer absorption curves for 2.5×10^{-5} M and 4.0×10^{-5} M solutions, obtained with 1-mm-thick sample cells and using a reference cell containing pure toluene. At the laser wavelength of 1052 nm, the respective transmissions are 0.83 and 0.74, giving absorption coefficients 1.86 cm^{-1} and 3.01 cm^{-1}, respectively. As a check on the dilution accuracy, these coefficients have a ratio 1.86/3.01 = 0.618, compared with the concentration ratio $2.5 \times 10^{-5}/4.0 \times 10^{-5}$ = 0.625. Using the absorption coefficient 3.01 cm^{-1} for the 4.0×10^{-5} M dye, the molecular ground state absorption cross section is calculated to be $\sigma_D = 1.25 \times 10^{-16}$ cm^2, which is nearly the same value found in Ref. 14 for BDN in polymethylmethacrylate.

Two types of dye cells were constructed. The first was made using two 1/2-in.-dia. glass windows separated by a thin cylindrical spacer ring 1.4 mm thick. The faces of the spacer ring were polished flat and parallel, and it was separated along a diameter by a slot in order to accommodate the filling and venting tubes. The windows, spacer sections, and tubes were fastened together with epoxy. The outer faces of the cell windows were antireflection coated, but the inner faces were left uncoated because the refractive index mismatch between the glass (~1.52) and the toluene solutions (~1.50) was so small. This cell was fastened to the output mirror holder with the stainless-steel fill tube at the bottom of the cell connected by Teflon tubing to a fill syringe containing the dye, and the top vent tube leading to a discharge collection flask. This arrangement allowed initial filling of the cell with toluene for optimum alignment, and then pumping and filling with dye solutions without disturbing the optical alignment.

The second type of cell was identical in construction to the first, except that the plane inner surface of one of the windows was dielectric coated to form the output mirror. Two cells of this type were made, having reflectivities of 0.80 and 0.75 with respect to the toluene filling medium.

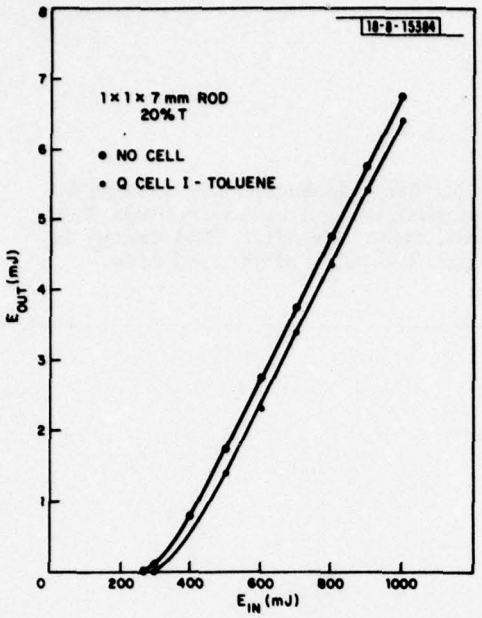

Fig. 33. Output vs input energy for 1- × 1- × 7-mm NPP rod in 10-cm confocal cavity with 20% transmitting output mirror. The open-circle data points are for the normal-mode cavity, and the closed-circle points are for the cavity with internal type I Q-switch cell containing pure toluene.

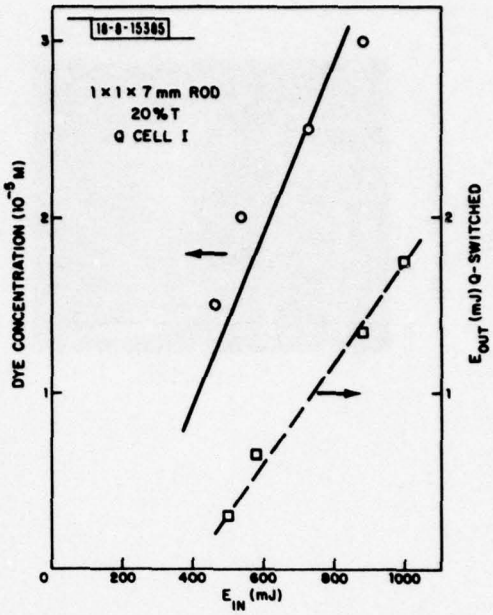

Fig. 34. Relation between Q-switch dye concentration (left scale) and threshold energy, and output energy (right scale) vs input energy for single-pulse, Q-switched output in a 1- × 1- × 7-mm NPP rod with confocal cavity.

The initial results using the type I dye cell with the 1- × 1- × 7-mm rod in the confocal resonator are shown in Figs. 33 and 34. The effects of adding the dye cell itself are shown in Fig. 33, where the operation with and without the toluene-filled cell are shown (the normal-mode data are the same as in Fig. 22). First, the data of Fig. 22 show a threshold increase of about 100 mJ per 10 percent cavity loss, and then from the data of Fig. 33 we estimate an added cell loss of about 3.5 percent. Note that this is too small to be evident in the slope efficiency, but is more apparent in the threshold shift with introduction of the dye cell. Next, in Fig. 34 we show (open circles, left scale) the threshold as a function of dye concentration in the cell. The calculated loss coefficient for the dye is 0.75 cm^{-1} per 10^{-5} M, or for the present cell, $2\alpha l$ = 0.21 per 10^{-5} M. The line shown through the data has a slope of 200 mJ per 10^{-5} M, or about 0.20 loss per 10^{-5} M, although the fit is not good, and differences between 2 αl and the round-trip loss $1-e^{-2\alpha l}$ are beginning to be significant. For a given concentration, multiple Q-switched pulses with separations on the order of tens of microseconds occurred when the input energy was too large. In measuring the single-pulse Q-switched energy output, we operated with an energy midway between the threshold and double-pulsing points for the most stable operation. In addition to the energy meter at the laser output end, we put a Si diode behind the HR mirror, which detected a weak output leaked through this mirror and was used to monitor and verify single-pulse operation during the energy measurements. The energy of the Q-switched pulses measured in this fashion as a function of pump energy is also plotted in Fig. 34 (open squares, right scale). With 1 J input, we obtained 1.75 mJ output using 3×10^{-5} M dye. This represents 27 percent of the 6.4-mJ normal-mode output measured with the cell

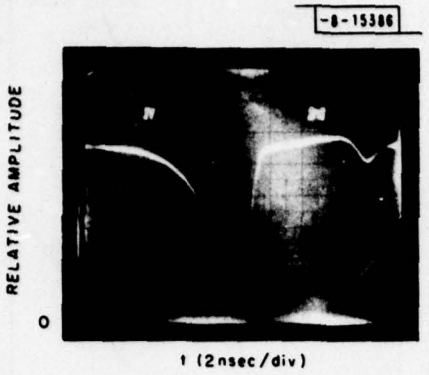

Fig. 35. Time dependence of Q-switched output pulse using a 1- × 1- × 7-mm NPP rod and confocal cavity. The energy is 1.75 mJ, and pulse width is ~7 nsec.

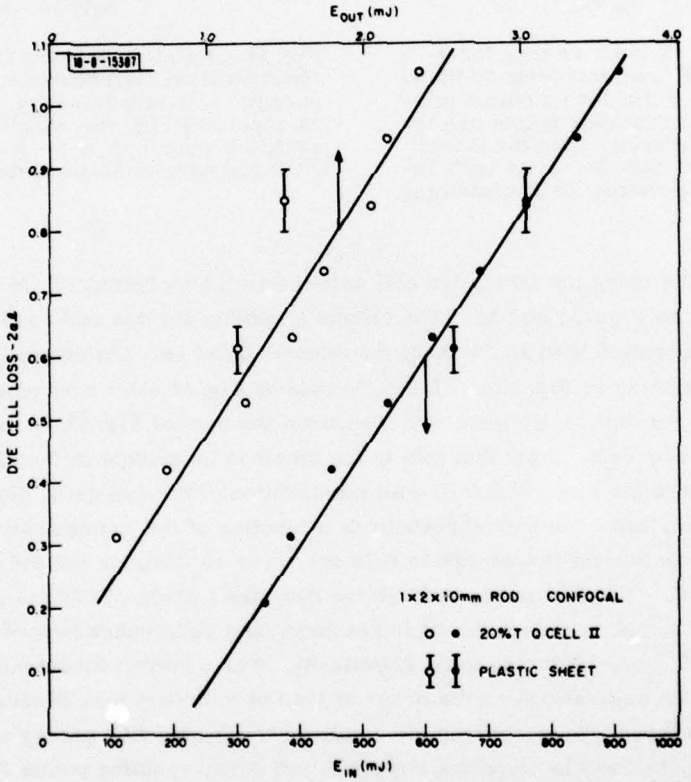

Fig. 36. Relation between Q-switch round-trip loss and threshold energy (bottom scale) and single-pulse output energy (top scale) for a 1- × 2- × 10-mm NPP rod in a confocal cavity.

containing toluene. The time dependence of the Q-switched pulse is shown in Fig. 35, as measured with a fast Si p-i-n photodiode and storage oscilloscope. The width of the pulse (FWHM) is ~7 nsec (we believe the small second pulse is a spurious signal probably due to an impedance mismatch).

In Fig. 36, we show similar data obtained with the 1- × 2- × 10-mm rod, using the same dye cell and confocal resonator. We have plotted the calculated dye-cell loss coefficient $2\alpha l$ (using dye concentrations up to 5×10^{-5} M) on the vertical axis, and the solid data points show the energy threshold (bottom scale) for varying loss. Even though we are in a regime where $2\alpha l$ is much greater than $1-e^{-2\alpha l}$, and even exceeds unity, the approximately linear relation is found because the gain coefficient $2gl$ which balances $2\alpha l$ is increasing roughly linearly with input energy. In other words, even in the high-gain regime, the round-trip gain $e^{2\alpha l}$ when multiplied by $e^{-2\alpha l}$ is a constant determined by the other fixed cavity losses. As before, the Q-switched output energy at each dye concentration was measured for a pump midway between the threshold and double-pulse level, but keeping E_{IN} less than 1 J. The data for output Q-switch energy (open circles, top axis) are shown for varying dye loss. At 1 J input with 5×10^{-5} M dye, we obtained 2.35 mJ output.

In addition to the liquid cell, we also used some plastic sheet Kodak Q-switch material (cellulose acetate containing BDN dye) provided by J. Gualtieri of USAERADCOM. Although no clear plastic sheet was available as a reference for the spectrophotometer transmission reference in order to separate intrinsic absorption loss from dielectric reflection loss, we estimate the absorption coefficients to be in the range given by the data points with brackets in Fig. 36. The thresholds and output energies are in moderately good agreement with the toluene-solvent Q-switch data, although we believe the poorer optical quality of the plastic sheet does result in larger internal laser loss and lower output. Using the more absorbing sheet, we obtained 1.5 mJ output at 925 mJ input.

In an effort to obtain single-mode, low-divergence output, we chose to use the type of cavity called a hybrid unstable resonator. Unstable resonators have the property that a geometric ray trace back and forth through the laser cavity eventually leads to the ray exiting from the cavity around the edge of an output coupler. The most common types of such resonators have high-reflectance mirrors and either use the annular output from around one of the end mirrors or insert a scraper mirror within the cavity to deflect this annular output. The ray-trace concept is equivalent to that of expanding spherical waves which have the desirable feature of filling the gain medium and extracting most of the energy within the cavity. To avoid the difficulties associated with fabricating and mounting an edge-coupled output mirror or introducing an additional scraper mirror, the hybrid unstable resonator was introduced for producing uniform low-divergence output in small Nd:YAG laser rangefinder cartridges.[17] In this design, one mirror is partially transmitting, giving a uniform beam, with the outer portion of beam corresponding to the conventional annular output being blocked or neglected.

The formulas given in Ref. 17 for estimating the magnification and geometric loss in the geometric (ray-tracing) approximation are

$$M = \frac{g^{1/2} + (g-1)^{1/2}}{g^{1/2} - (g-1)^{1/2}} \tag{40}$$

and

$$\delta = (1 - 1/M^2)^2 \tag{41}$$

where we have assumed a plane output mirror, and $g \approx 1 + L/R$, with L = cavity length and R = convex rear mirror radius of curvature. With the 10- and 20-m-radius mirrors, the calculated magnifications and edge losses are $M_{10} = 1.22$ and $\delta_{10} = 0.11$, $M_{20} = 1.15$ and $\delta_{20} = 0.06$.

Data for the hybrid unstable resonator (HUR) using a 1- × 2- × 10-mm rod are shown in Fig. 37 for normal-mode (non-Q-switched) operation. Contrary to the calculations, the 20-m mirror gave a slightly higher threshold and less energy output than the 10-m mirror, even though the theoretical geometric loss is less for the former. This may be related to differences in the equivalent-cavity Fresnel number, which is closer to a half-integer value for the 10-m mirror, which tends to reduce the geometric loss. The experimental results with the 10-m mirror were nearly identical with either the 21% T output mirror or the 20% T type II Q-switch cell. There was a significant reduction in the output compared with that of the stable confocal resonator (Fig. 23), which may be partly due to the geometric loss causing higher threshold and lower efficiency.

The data for Q-switched operation using the HUR are shown in Fig. 38, presented in the same manner as in Fig. 36 for the stable confocal resonator. With an input energy of 925 mJ we obtained 1.2 mJ Q-switched output using 5×10^{-5} M dye. This is about 20 percent of the corresponding normal-mode HUR output, and about half of the stable resonator Q-switched output.

Using a larger cross section 2- × 2- × 10-mm rod and greater input energies, the HUR normal mode data of Fig. 39 were obtained. With the type II Q cell, 18 mJ output occurred at 2 J input, compared with 34.5 mJ in the confocal resonator (Fig. 25). When Q-switched using the 25% T type II cell, we obtained 5.15 mJ output at 1.86 J input (Fig. 40).

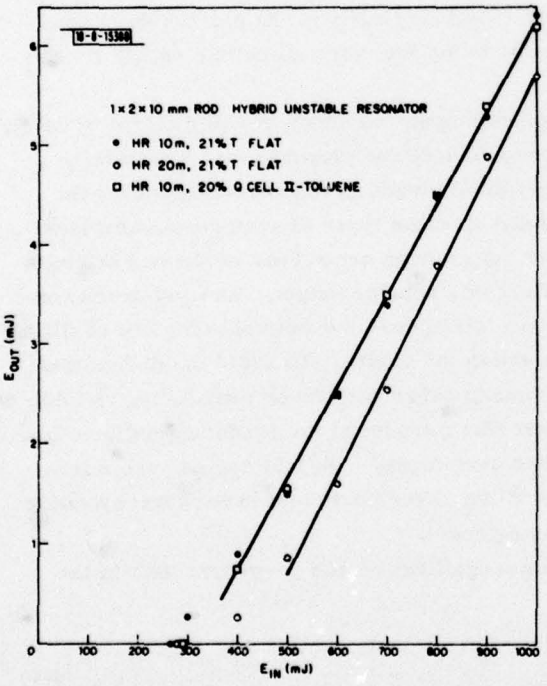

Fig. 37. Output vs input energy for normal-mode operation of a 1- × 2- × 10-mm NPP rod in a hybrid unstable resonator.

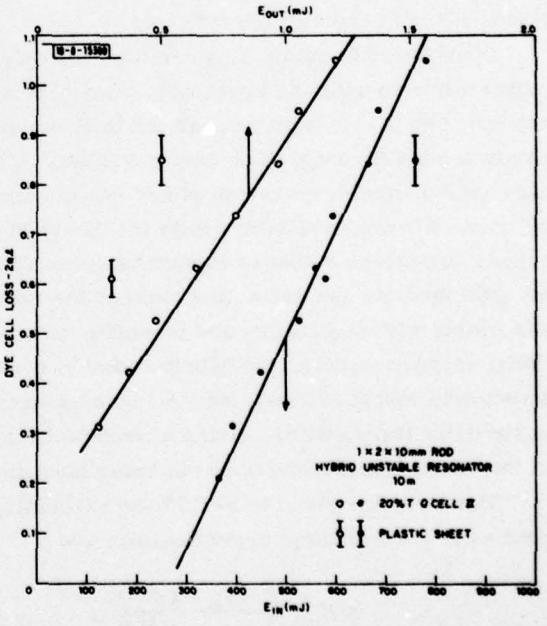

Fig. 38. Relation between Q-switch round-trip loss and threshold energy (bottom scale) and single-pulse output energy (top scale) for a 1- × 2- × 10-mm NPP rod in a hybrid unstable resonator.

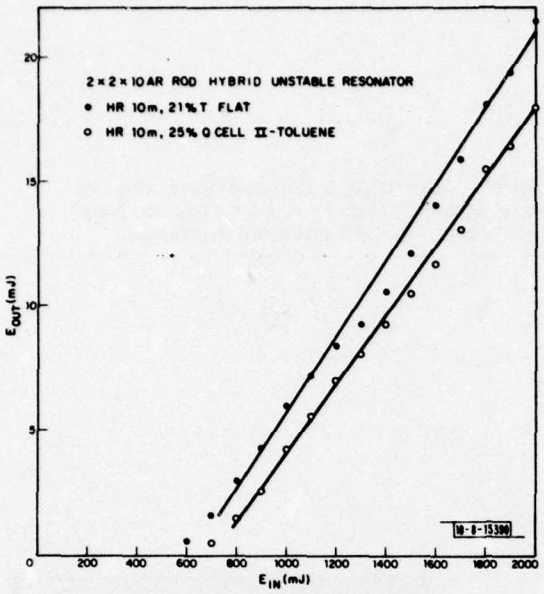

Fig. 39. Output vs input energy for normal-mode operation of a 2- × 2- × 10-mm NPP rod in a hybrid unstable resonator.

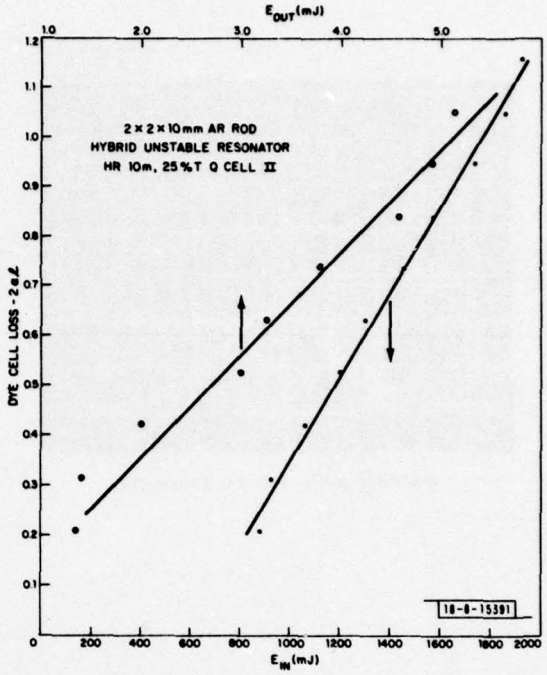

Fig. 40. Relation between Q-switch round-trip loss and threshold energy (bottom scale) and single-pulse output energy (top scale) for a 2- × 2- × 10-mm NPP rod in a hybrid unstable resonator.

Far-field measurements of the HUR output were performed using two techniques. In one, the Scientech power meter head was placed 6.4 m (21 ft) from the laser with a variable iris in front, and "energy-in-the-bucket" measurements were done, with the divergence angle being calculated from the aperture opening. The other method used an infrared display measurement similar to that for the near-field fluorescence. In this case, a target with calibration grid was placed at the far-field iris position and the vidicon camera was focused on the target and incident laser spot. The image of the spot was displayed on the TV monitor and scanned with the CVI video analyzer to give a quantitative profile of the mode.

In principle, one should use a collimating lens at the laser output to compensate for the geometric divergence of the beam, which has a radius of curvature[17]

$$R_c = \sqrt{L^2 + LR_{mirror} + z} \qquad (42)$$

where

R = convex mirror radius

z = distance from output mirror .

At z = 0, the calculated radius is $\sim\sqrt{10\text{ cm} \times 1000\text{ cm}}$ = 1 m requiring a 1-m lens for collimation. We did not have this long-focal-length lens available, and, in any event, the calculated Fresnel diffraction pattern did not differ significantly with or without the lens since the calculated geometric divergence is small compared with diffraction.

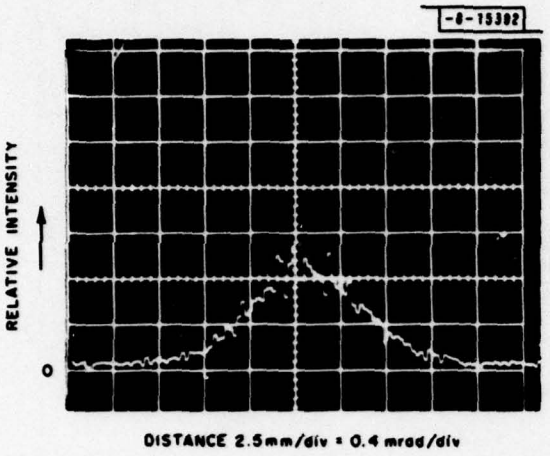

Fig. 41. Far-field video analyzer scan of mode pattern from 1- × 2- × 10-mm NPP laser rod in hybrid unstable resonator.

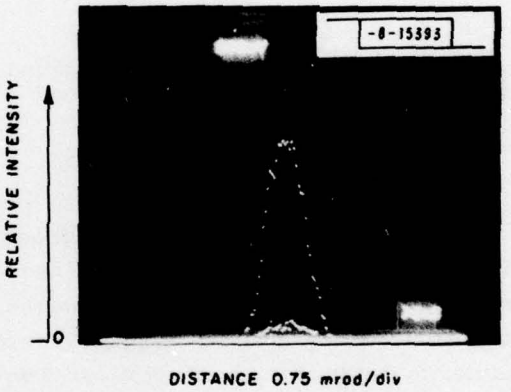

Fig. 42. Far-field video analyzer scan of mode pattern from 2- × 2- × 10-mm NPP laser rod in hybrid unstable resonator (top) and time dependence of the Q-switched output (bottom).

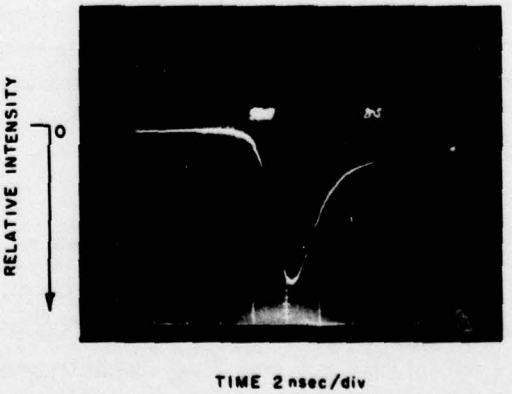

A typical far-field scan is shown in Fig. 41. This particular pattern was obtained with normal-mode operation of the 1- × 2- × 10-mm rod in the HUR using the 10-m mirror and type II toluene-filled dye cell with 20% transmission. The spatial calibration was found from a separate CVI scan of the illuminated grid pattern on the screen. Most of the energy falls within a 2.4-mrad angle, or a 1.5-cm spot diameter. The calculated spot size for a 1-mm source is 1.2 cm for a diffraction-limited beam. The observed spot does not exhibit the expected diffraction lobes, although these should be less than 5 percent of the peak amplitude, and also appears to be symmetric, even though the rod cross section is rectangular. Using the power meter for this same measurement gave energies of 6.0 mJ in the near field and 4.8 mJ and 5.3 mJ in 2.3- and 2.7-mrad apertures, respectively. Under the same conditions which previously gave 1.05 mJ Q-switched output in the near field, we obtained 0.75 mJ in 3 mrad in the far field, with a scan pattern almost identical to Fig. 41. This Q-switched output was more erratic in that the spot shape or mode pattern was occasionally quite asymmetric, although its general size remained the same.

The same measurements were repeated for the 2- × 2- × 10-mm AR rod (near-field data of Fig. 40). At the beginning of the measurements, alignment for maximum near-field energy gave 5.5 mJ Q-switched output at 1.92 J in. However, the far field showed a double-lobed pattern. When the alignment was adjusted to give a symmetric far-field output, we obtained 3.9 mJ in a 3.1-mrad aperture. The CVI far-field scan of this output is shown at the top of Fig. 42, and the time behavior is shown at the bottom (6 nsec FWHM).

IV. SUMMARY AND CONCLUSIONS

As the first part of this study, we have experimentally measured the anisotropic thermal conductivity and specific heat of pure NdP_5O_{14}. With these parameters, in principle, it is possible to calculate the time- and space-dependent temperature distribution of NPP laser rods, given the heating function found from the pump absorption and the boundary conditions for cooling the rod. We may not be able to specify these quantities precisely, because of effects such as convective heating and cooling of the rod and the complex geometry of the pump absorption, but nevertheless, simple approximations should give good semi-quantitative predictions of the heating to be expected. The next important step should be to calculate and measure how such heating affects both the lasing performance and the crystal integrity of the laser rod.

The lasing performance is affected by temperature from both intrinsic fluorescence properties and macroscopic optical properties. The two dominant processes affecting the intrinsic ionic fluorescence properties are the increase in thermal population of the $^4I_{11/2}$ manifold, requiring a larger $^4F_{3/2}$ population inversion, and the increased linewidth of the lasing transition at higher temperatures, lowering the effective laser cross section and gain. For a uniform temperature rise, the first factor would cause a practical change in the resonant loss term of $(\Delta E/kT)(1/T)$ which at room temperature is approximately 3%/°C. Since the round-trip resonant loss itself is about 5%/cm, a temperature rise on the order of 20°C would be necessary to make a significant change in laser performance, since the output coupling should far exceed the resonant loss. The transitions in NPP are predominantly homogeneously broadened from a phonon Raman scattering process. The theoretical linewidth is proportional to T^2, giving a fractional decrease in the laser cross section or gain of 2/T or 0.7%/°C at room temperature. This slight decrease should be offset to some extent from the increased overlap of adjacent transitions which contribute to the gain at a given wavelength near the R_1-Y_1 dominant peak. If operation of the laser is required at temperature exceeding 50°C, it may be necessary to incorporate temperature-compensation circuitry or other means to avoid or allow for multiple Q-switched pulsing which could occur at the low-temperature extreme, where the laser gain would be higher and loss lower.

The other direct thermal effects on laser performance arise from changes in the macroscopic optical properties such as the index of refraction. In Nd:YAG, which because of its cubic symmetry possesses no intrinsic birefringence, thermal gradients lead to thermally induced birefringence which limits the mode quality and output power. In NPP, the intrinsic birefringence is significant, so that the polarization properties are unlikely to be affected by temperature changes. However, the large thermal gradients may cause changes in the highest gain index component, n_b, large enough to lead to thermal focusing or defocusing effects in the rod, changing the effective resonator parameters and output divergence. Some initial measurements of the change in optical path length with temperature have been reported, but the individual contributions of dn/dT and dl/dT have not been determined.

This latter property is also important in determining the mechanical behavior of the laser rod as its temperature changes. To avoid straining the rod, the thermal expansion coefficients of the mount should match those of the rod. In view of the large anisotropy of the thermal conductivity, some degree of anisotropy in the thermal expansion should be expected and the mount designed accordingly if it is to operate over a wide temperature range. In addition to the possible strains produced at the rod-mount interface, it may also be necessary to examine the

stresses induced within the rod from a combination of thermal gradients and anisotropic thermal expansion under extreme operating conditions.

Our ab initio calculations of the time-dependent NPP laser output give good qualitative agreement with the experimental results. The quantitative differences arise from the unknown parameters of the system, primarily the exact absorption geometry and the transverse laser mode distribution. Because the absorption coefficients are large in NPP, both of these factors are critical in determining the laser behavior, as demonstrated by the calculated results for a slightly reduced mode size. Improvements to the calculations could be made by more accurate modeling of the time-dependent lamp radiation and by calculating the rate-equation solutions in the high-gain regime, but in view of the previously mentioned unknown quantities, this would probably serve little purpose.

Experiments with the flash-lamp-excited NPP lasers have demonstrated the capability of such devices to provide several millijoules of Q-switched energy in a beam with less than 4 mrad divergence. These parameters do not fully demonstrate the capability of such lasers, since many aspects of the laser operation were not optimized. In order to summarize the results with a view toward extrapolating the final device potential, we shall review some of the separate aspects of the laser performance. First, a minimum value of normal-mode energy conversion of 2.1 percent total (2.5 percent differential) has been demonstrated with a 2- × 2- × 20-mm rod operating at 3.3 J input, 70 mJ output. This result was obtained in a confocal resonator aligned for uniform, multimode output with an uncoated rod. Other measurements have shown no differences between uncoated rods and rods that had anti-reflection coatings. These were equivalent in the sense that coating did not reduce any intracavity losses, as determined from the laser threshold and output efficiency. However, from the behavior of the 2- × 2- × 20-mm rod at the highest pump levels, it appears that anti-reflection coating may be necessary to suppress laser oscillation from an uncoated facet. With such coating, an output of 88 mJ at 4 J input should be attainable.

This output might be improved by redesign of the laser head to provide more uniform illumination of the laser rod and a more uniform gain distribution within the rod. Techniques such as use of elliptical focusing might prove effective, at the cost of a slightly larger head cross section. Although our initial experiments with dual-lamp excitation were inconclusive, proper design of such a laser head should also be effective in yielding more uniform inversion.

Another area of improvement is in the design of the hybrid unstable resonator. A comparison of the data in Figs. 26 and 39, for example, shows a differential efficiency of 2 percent for the confocal resonator and 1.5 percent for the hybrid unstable resonator, with the HUR having 60 percent of the confocal output. This HUR output is a near-field measurement, and, typically, 85 percent of this is collected in a 3-mrad aperture in the far field, reducing the slope efficiency and relative output to 1.3 and 50 percent, respectively. If one uses the calculated geometric loss factor of 11 percent, the theoretical maximum relative efficiency should be $T/L + T = 0.20/(0.11 + 0.20) = 65$ percent. Different resonator parameters or an improved design, possibly using a conventional unstable resonator with a small-reflecting-area output coupler, should be investigated. It should be feasible to extract ~75 percent of the multimode output in a diffraction-limited beam, for an estimated 66 mJ output at 4 J input in normal-mode operation.

The major remaining problem is extraction of the normal-mode, long-pulse energy in a short Q-switched pulse. This problem has been examined in a more general analytic fashion[17] by considering the losses from the Q-switch in the initial unbleached state and above threshold

in the saturated state. Our approach has been somewhat more empirical, but more quantitative since these two dye loss terms have been treated as dynamic variables in the laser rate equations, and the integrated effect of the time-varying loss has been found. The particular data of Fig. 21 show that roughly 0.4 to 0.5 of the normal-mode output should be achievable for the present type of saturable-absorber dye. In practice (Figs. 39 and 40), this ratio is about 5 mJ/18 mJ = 0.28 (near field). One factor which could cause a reduction in Q-switch efficiency is the nonuniformity of the laser mode, which could prevent full dye saturation at the mode periphery. Assuming this Q-switch efficiency factor to be 0.3, a predicted energy output is then 0.3×66 mJ = 20 mJ at 4 J input. Therefore, for this goal of 20 mJ in a diffraction-limited Q-switch pulse to be reached, one must have a minimum reduction factor of ~0.25 of the experimentally measured 80-mJ long-pulse multimode energy. In our experiments, this overall measured reduction factor is ~4 mJ/35 mJ = 0.11, so an improvement of about 40 percent is necessary in both the HUR and Q-switch efficiencies.

Effects of the dye cells on the mode divergence have not been measured. Nonlinear index changes related to the dye bleaching may act as an internal lens, affecting the far-field output, and should be considered in choosing the dye cell parameters of length and concentration. Another influence on these parameters is the possibility of optical damage. In one case where a semi-concentric cavity was tested, the small mode area at the dye cell position caused visible damage to the cell. Examination under a microscope showed that the damage occurred at the inner, uncoated window-dye interface and presumably resulted from destructive absorption by the dye, with possible combined effects of high thermal loading and chemical decomposition causing damage spots on the glass surface. While this was an extreme case, with a power density much higher than would be reached in a non-focused mode, it indicates the possibility of infrared damage to the dye if energy absorption density is too large. Such a situation might be reached for example in thin cells with high dye concentration, even for non-focused modes.

Another necessary step is the improvement of the optical quality of the plastic sheet dye Q-switches. Experimentally, they have yielded only 0.50 to 0.75 of the energies obtained with comparable density liquid Q-switch cells. Likely causes of this reduction are poorer surface flatness and parallelism and material inhomogeneities in the plastic sheet. Since the plastic sheet we used was not AR coated, the non-parallelism and misalignment of the sheet may also have introduced internal losses to the laser.

Although our calculations have shown that the maximum Nd concentration is required for the most efficient lasing performance, this result may not be true with combined effects of reduced mode size and intensity-dependent Q-switch loss. The slight loss in overall absorption efficiency with lower Nd concentration may be offset by the increased gain uniformity in the laser rod and its effect on the mode profile. Unfortunately, the calculation of an unstable resonator mode with non-uniform gain is quite complex, and at the present, there are no (Nd, La)PP laser rods for obtaining experimental data.

APPENDIX

GREEN'S FUNCTION SOLUTION OF THE ANISOTROPIC HEAT FLOW EQUATION

The solution of the heat-flow equation (1) can be found by integrating the solution to the Green's function equation (2) over the time- and space-dependent heating source function. The solution to (2) is found as follows. Let the spatial Fourier transform of G equal $\Gamma(\vec{p})$. Then

$$(\Lambda_x p_x^2 + \Lambda_y p_y^2 + \Lambda_z p_z^2)\,\Gamma + \rho C \frac{\partial \Gamma}{\partial t} = 4\pi\delta(\tau) \tag{A1}$$

where $\tau = t - t_o$. The solution of Eq. (A1) is

$$\Gamma = u(\tau)\,\frac{4\pi}{\rho C}\,\exp\left\{-\frac{[\Lambda_x p_x^2 + \Lambda_y p_y^2 + \Lambda_z p_z^2]}{\rho C}\,\tau\right\} \quad . \tag{A2}$$

The solution G is the inverse transform of Γ,

$$G(r,\tau) = \frac{4\pi}{\rho C}\,\frac{u(\tau)}{(2\pi)^3}\int_{-\infty}^{\infty} e^{i\vec{p}\cdot\vec{r}}\,\Gamma(\vec{r},\tau)\,d\vec{r} \quad , \tag{A3}$$

where, for example, the contribution to the factorable integral from the x component is

$$I_x = \int_{-\infty}^{\infty} e^{ip_x x}\,e^{-\Lambda_x p_x^2 \tau/\rho C}\,dp_x = e^{\frac{-\rho C x^2}{\Lambda_x 4\tau}}\sqrt{\frac{\pi\rho C}{\tau\Lambda_x}} \quad . \tag{A4}$$

Using similar results for the y and z coordinates,

$$G(r,\tau) = \frac{1}{2}\sqrt{\frac{\rho C}{\pi\tau^3}}\,\frac{u(\tau)}{\sqrt{\Lambda_x\Lambda_y\Lambda_z}}\,\exp\left[-\frac{\rho C}{4\tau}\left(\frac{x^2}{\Lambda_x} + \frac{y^2}{\Lambda_y} + \frac{z^2}{\Lambda_z}\right)\right] \quad . \tag{A5}$$

This solution is the impulse response to a point-source excitation at $\tau = t - t_o = 0$ so that for a sinusoidal driving function we must perform the convolution over $\cos\omega t_o$,

$$T(r,t) = \int_{-\infty}^{t} \frac{P_o}{4\pi}\cos\omega t_o\,G(t - t_o)\,dt_o \quad . \tag{A6}$$

With the change of variable

$$\xi^2 = \frac{\rho C}{4}\left(\frac{x^2}{\Lambda_x} + \frac{y^2}{\Lambda_y} + \frac{z^2}{\Lambda_z}\right)\frac{1}{t - t_o} \quad ,$$

the integration over ξ gives

$$T(r,t) = \frac{P_o}{4\pi}\left(\frac{x^2}{\Lambda_x} + \frac{y^2}{\Lambda_y} + \frac{z^2}{\Lambda_z}\right)^{-1/2}(\Lambda_x\Lambda_y\Lambda_z)^{-1/2}\,\mathrm{Re}\left[\exp\left(i\omega t - \sqrt{i\omega\rho C}\right.\right.$$
$$\left.\left.\times\sqrt{\frac{x^2}{\Lambda_x} + \frac{y^2}{\Lambda_y} + \frac{z^2}{\Lambda_z}}\right)\right] \quad . \tag{A7}$$

This is the solution for a time-periodic point-source distribution, which must be integrated to find the response from the present line source. In our geometry, the line source lies in the

plane at z = 0, and extends in the y direction. The temperature sensor is located a distance "d" from the heater source, and is also in the plane at z = 0. Since "d" is very much less than the heater length, we will neglect edge effects, and take the limits of y integration from $-\infty$ to $+\infty$. The line-source response is

$$T(d,t) = \frac{P_o}{4\pi} \frac{Re}{\sqrt{\Lambda_x \Lambda_y \Lambda_z}} \int_{-\infty}^{\infty} dy \left(\frac{d^2}{\Lambda_x} + \frac{y^2}{\Lambda_y}\right)^{-1/2}$$

$$\times \exp\left\{i\omega t - \left[i\omega\rho C\left(\frac{d^2}{\Lambda_x} + \frac{y^2}{\Lambda_y}\right)\right]^{1/2}\right\} \quad . \tag{A8}$$

Using the change of variable

$$\xi = \sqrt{\frac{y^2}{d^2}\frac{\Lambda_x}{\Lambda_y} + 1} \quad ,$$

this becomes

$$T(d,t) = \frac{P_o}{2\pi} \frac{1}{\sqrt{\Lambda_x \Lambda_z}} Re\left\{e^{i\omega t} \int_1^{\infty} \frac{d\xi}{\sqrt{\xi^2 - 1}} \exp\left[-\sqrt{\frac{i\omega\rho C}{\Lambda_x}}\, d\xi\right]\right\} \tag{A9}$$

$$= \frac{P_o}{2\pi} \frac{1}{\sqrt{\Lambda_x \Lambda_z}} Re\left\{e^{i\omega t} K_o\left(\sqrt{\frac{i\omega\rho C}{\Lambda_x}}\, d\right)\right\} \quad , \tag{A10}$$

from the integral definition of the modified Bessel function, K_o.

The actual heater and sensors are not lines of zero thickness, but have some finite width w. When this factor is integrated as in Ref. 5, an additional factor of $[\sinh(\alpha w/2)/(\alpha w/2)]^2$ is found using arguments as above, where the factor α now has the anisotropic tensor element of the thermal conductivity,

$$\alpha = (i\omega\rho C/\Lambda_x)^{1/2} \tag{A11}$$

and the voltage response of the sensor is

$$V_\omega = \frac{V\beta P}{\pi\sqrt{\Lambda_x \Lambda_z}} K_o(\alpha d) \left[\frac{\sinh(\alpha w/2)}{(\alpha w/2)}\right]^2 \tag{A12}$$

with all quantities defined as in Eq. (6). Although both the magnitude and phase of V_ω are measured, it suffices to use only the magnitude in determining the unknowns α and Λ_i:

$$|V_\omega| = \frac{V\beta P}{\pi\sqrt{\Lambda_x \Lambda_z}} \left[\frac{\sinh^2(|\alpha| w/2\sqrt{2}) + \sin^2(|\alpha| w/2\sqrt{2})}{(|\alpha| w/2)^2}\right] |K_o(\alpha d)| \quad . \tag{A13}$$

The numerical calculation of K_o is found using the series expansions of Ref. 18,

$$K_o(z) = -[\log(z/2) + \gamma] I_o(z) + \sum_{m=1}^{\infty} \frac{(z^2/4)^m}{(m!)^2} \left(1 + \frac{1}{2} + \ldots + \frac{1}{m}\right) \tag{A14}$$

where the modified Bessel function $I_o(z)$ can be found from

$$I_o(z) = \sum_{m=0}^{\infty} \frac{(z^2/4)^m}{(m!)^2}$$

and

$$\gamma = \text{Euler's constant} = 0.57721\ldots \quad . \tag{A15}$$

In our calculations, the complex argument z is of the form $\sqrt{i}\ v$, with v real, so we will determine the real and imaginary parts of the Bessel functions with this choice of variable. From Eq. (A14) we define

$$S(z) = \sum_{m=1}^{\infty} \frac{(z^2/4)^m}{(m!)^2} \left(1 + \frac{1}{2} + \ldots + \frac{1}{m}\right) \quad , \tag{A16}$$

giving

$$S(z) = i \sum_{m=0}^{\infty} \frac{(v^2/4)^{2m+1}\,(-1)^m}{(2m+1!)^2} \left(1 + \frac{1}{2} + \ldots \frac{1}{2m+1}\right)$$

$$+ \sum_{m=1}^{\infty} \frac{(v^2/4)^{2m}\,(-1)^m}{(2m!)^2} \left(1 + \frac{1}{2} + \ldots + \frac{1}{m}\right) \tag{A17}$$

$$= i\ \text{Im}\ S + \text{Re}\ S$$

and

$$I_o(z) = \sum_{m=0}^{\infty} \frac{(v^2/4)^{2m}\,(-1)^m}{(2m!)^2} + i\,\frac{v^2}{4} \sum_{m=0}^{\infty} \frac{(v^2/4)^{2m}\,(-1)^m}{(2m+1!)^2} \tag{A18}$$

$$= \text{Re}\ I_o + i\ \text{Im}\ I_o \quad .$$

For computational purposes we define the quantities

$$f_m = \frac{1}{(m!)^2} \qquad c_m = \frac{1}{(m!)^2} \left(\frac{1}{1} + \frac{1}{2} + \ldots + \frac{1}{m}\right)$$

$$v^2/4 = y \qquad y^2 = x$$

so that the above functions can be put into the following forms for efficient numerical analysis:

$$I_o(z) = 1 - x(f_2 - x(f_4 - x(f_6 \ldots))) + iy\,[f_1 - x(f_3 - x(f_5 - x(\ldots)))]$$

$$S(z) = -x(c_2 - x(c_4 - \ldots)) \qquad + iy\,[c_1 - x\,(c_3 - x(c_5 - x(\ldots)))] \quad , \tag{A19}$$

where sufficient terms are taken to insure convergence. Then,

$$K_o(z) = -(\log(v/2) + \gamma)\ \text{Re}\ I_o + \frac{\pi}{4}\ \text{Im}\ I + \text{Re}\ S$$

$$+i\,[-(\log(v/2) + \gamma)\ \text{Im}\ I - \pi/4\ \text{Re}\ I + \text{Im}\ S] \quad , \tag{A20}$$

and

$$|K_o(z)| = [(\text{Re}\ K_o)^2 + (\text{Im}\ K_o)^2]^{1/2} \quad . \tag{A21}$$

REFERENCES

1. H. P. Weber, Optical and Quantum Electron. 7, 431 (1975).
2. S. R. Chinn, J. W. Pierce, and H. Heckscher, Appl. Opt. 15, 1444 (1976).
3. W. K. Zwicker, T. Kovats, and S. R. Chinn, Fifth International Conference on Crystal Growth, Boston, Massachusetts, 1977, paper no. 237.
4. S. R. Chinn and W. K. Zwicker, Appl. Phys. Lett. 31, 178 (1977).
5. R. H. Bruce and D. S. Cannell, Rev. Sci. Instrum. 47, 1323 (1976).
6. G. Bäckström and J. Chaussy, J. Phys. E 10, 767 (1977).
7. H. Y-P. Hong, Acta Cryst. B 30, 468 (1974).
8. H. S. Carslaw and J. C. Jaeger, Conduction of Heat in Solids (Oxford, London, 1959), Sec. 1.17.
9. P. M. Morse and H. Feshbach, Methods of Theoretical Physics (McGraw-Hill, New York, 1953), Sec. 7.4.
10. P. H. Klein and W. J. Croft, J. Appl. Phys. 38, 1603 (1967).
11. W. Koechner, Solid-State Laser Engineering (Springer-Verlag, New York, 1976), Chap. 7.
12. H. Eichler, G. Salje, and H. Stahl, J. Appl. Phys. 44, 5383 (1973).
13. J. P. Markiewicz and J. L. Emmett, IEEE J. Quantum Electron. QE-2, 707 (1966).
14. F. Kobylarz, R. H. Wright, H. Saphow and N. Yeamans, Proceedings of 6th Department of Defense Conference on Laser Technology, U.S. Air Force Academy, Colorado Springs, Colorado, 1976.
15. K. H. Drexhage and U. J. Müller-Westerhoff, IEEE J. Quantum Electron. QE-8, 759 (1972).
16. Linear Xenon Flashtubes, Data Sheet F1002C-2, EG&G Electro-Optics Division, Salem, Massachusetts; Air-cooled Linear Flashlamp Catalog, Bulletin 1524, ILC Technology, Sunnyvale, California.
17. A. C. Safyurtlu, "Unstable Resonator Laser Cartridge Development Study," ERADCOM Technical Report DELNV-76-0856-1 (1978).
18. M. Abramovitz and I. Stegun, Handbook of Mathematical Functions (Dover, New York, 1968).

UNCLASSIFIED

SECURITY CLASSIFICATION OF THIS PAGE *(When Data Entered)*

REPORT DOCUMENTATION PAGE

READ INSTRUCTIONS BEFORE COMPLETING FORM

1. REPORT NUMBER: ESD-TR-78-392	2. GOVT ACCESSION NO.
3. RECIPIENT'S CATALOG NUMBER	
4. TITLE *(and Subtitle)*: Research Studies on Neodymium Pentaphosphate Miniature Lasers,	5. TYPE OF REPORT & PERIOD COVERED: Final Report · 1 Oct 1977 – 30 Sep 1978
	6. PERFORMING ORG. REPORT NUMBER
7. AUTHOR(s): Stephen R. Chinn	8. CONTRACT OR GRANT NUMBER(s): F19628-78-C-0002
9. PERFORMING ORGANIZATION NAME AND ADDRESS: Lincoln Laboratory, M.I.T. P.O. Box 73 Lexington, MA 02173	10. PROGRAM ELEMENT, PROJECT, TASK AREA & WORK UNIT NUMBERS: Program Element No. 61000A
11. CONTROLLING OFFICE NAME AND ADDRESS: United States Army Electronic Research and Development Command Fort Monmouth, NJ 07703	12. REPORT DATE: 30 September 1978
	13. NUMBER OF PAGES: 64
14. MONITORING AGENCY NAME & ADDRESS *(if different from Controlling Office)*: Electronic Systems Division Hanscom AFB Bedford, MA 01731	15. SECURITY CLASS. *(of this report)*: Unclassified
	15a. DECLASSIFICATION DOWNGRADING SCHEDULE

16. DISTRIBUTION STATEMENT *(of this Report)*

Approved for public release; distribution unlimited.

17. DISTRIBUTION STATEMENT *(of the abstract entered in Block 20, if different from Report)*

18. SUPPLEMENTARY NOTES

None

19. KEY WORDS *(Continue on reverse side if necessary and identify by block number)*

neodymium pentaphosphate
flash-lamp-excited laser rods
laser resonator parameters
miniature laser
laser rate equations
differential scanning calorimetry
Q-switched operation

20. ABSTRACT *(Continue on reverse side if necessary and identify by block number)*

The thermal conductivity and specific heat of NdP_5O_{14} have been measured using a dynamic electrical heating technique. The values of the thermal conductivity tensor elements (in W/cm-K) are $A_a = 2.10 \times 10^{-2}$, $A_b = 9.66 \times 10^{-3}$, and $A_c = 1.40 \times 10^{-2}$. The specific heat is 0.141 cal/g-K, in excellent agreement with the value of 0.139 cal/g-K that was measured by differential scanning calorimetry.

Using the experimentally measured thermal properties, we have calculated the time-dependent heating effects of typical flash-lamp-excited round and rectangular laser rods. With repetition rates limited to ~10 ppm, simple conductive cooling by an ambient-temperature heat-sink should be adequate.

Computer simulation of the flash-lamp-excited NPP laser has been carried out by numerical solution of the laser rate equations. With 1 J electrical input, typical calculated output energies are 24 mJ for normal-mode operation and 10 mJ for passively Q-switched operation. Optimum Q-switch absorption and output mirror transmission have also been calculated.

Experimental studies of such lasers have been made with varying laser rod size and laser resonator parameters. With the largest rod, $2 \times 2 \times 20$ mm^3, we have obtained 72 mJ output with 3.4 mJ input, in a normal-mode confocal resonator. Passive Q-switching of $2 \times 2 \times 10$ mm^3 rods in a hybrid unstable resonator has produced 5 mJ near-field output (2 J input) in a 6-nsec pulse, with 3.9 mJ collected in a 3.1-mrad far-field aperture.

DD FORM 1 JAN 73 1473 EDITION OF 1 NOV 65 IS OBSOLETE

UNCLASSIFIED

SECURITY CLASSIFICATION OF THIS PAGE *(When Data Entered)*

207 650